

Spatially-dependent modeling and simulation of runaway electron mitigation in DIII-D

M. T. Beidler,* D. del-Castillo-Negrete, L. R. Baylor, D. Shiraki, and D. A. Spong
Oak Ridge National Laboratory, Oak Ridge, Tennessee 37831-8071, USA

New simulations with the Kinetic Orbit Runaway electron (RE) Code KORC show RE deconfinement losses to the wall during plasma scrape off are the primary current dissipation mechanism in DIII-D experiments with high-Z impurity injection, and not collisional slowing down. The majority of simulations also exhibit an increase in the RE beam energy due to acceleration by the induced toroidal electric field, even while the RE beam current is decreasing. In this study, KORC integrates RE orbits using the relativistic guiding center equations of motion, and incorporates time-sequenced, experimental reconstructions of the magnetic and electric fields and line integrated electron density to construct spatiotemporal models of electron and partially-ionized impurity transport in the companion plasma. Comparisons of experimental current evolution and KORC results demonstrate the importance of including Coulomb collisions with partially-ionized impurity physics, initial RE energy, pitch angle, and spatial distributions, and spatiotemporal electron and partially-ionized impurity transport. This research provides an initial quantification of the efficacy of RE mitigation via injected impurities, and identification of the critical role played by loss of confinement due to plasma scrape off on the inner wall as compared to the relatively slow collisional damping.

I. INTRODUCTION

If not avoided or dissipated, runaway electrons (REs) can seriously damage ITER's plasma-facing components [1, 2]. If avoidance fails, shattered pellet injection (SPI) is the leading candidate to dissipate REs in ITER [3–6], and although significant progress has been made, there is a pressing need for modeling and simulation studies to assess the efficacy of SPI and to optimize different dissipation strategies, such as massive gas injection (MGI). From the theory and simulation perspective, there is a need to develop and validate realistic models of the interaction of REs with partially-ionized impurities, such as those proposed in Refs. [7, 8].

Recent experiments at DIII-D indicate that SPI and MGI perform similarly [9]. This work will focus on DIII-D discharge #164409, which has been reported extensively in Ref. [9]. The evolution of characteristic parameters are plotted in Fig. 1. At approximately 1.2 s, a small Ar pellet is injected that triggers the observed current quench in Fig. 1a. A RE beam is generated and position controlled until a secondary injection of Ne gas at approximately 1.4 s (marked by the vertical, dashed line) causes the RE beam to dissipate. Figure 1b shows three vertical, interferometer chords, capturing the evolution of line integrated electron density. Figure 1c shows the inferred toroidal electric field from the loop voltage measured at the high field side (HFS) and low field side (LFS). The bremsstrahlung hard x-ray (HXR) signals in Fig. 1d are measured by a bismuth-germanate based scintillator located at the bottom of DIII-D and mostly sensitive to 1–10 MeV photons [10]. The RE plateau phase is significantly different from the pre-disruption, in that the majority of the current is carried by REs and not by the cold ($T_e < 2$ eV) “companion”, or background, plasma [11, 12]. For this reason, the dynamics during this phase can be well studied using a particle tracking code, and in this work we employ the Kinetic Orbit Runaway electrons Code (KORC) [13]. The data in Fig. 1

will be both used as inputs to KORC calculations as described in Sec. II, and compared to outputs from KORC calculations in Sec. IV.

There have been significant previous efforts to model RE dissipation by impurity injection. Refs. [14–16] use 1D transport codes with Fokker-Planck models for REs having physics of bound electrons and partially-ionized impurities. Ref. [17] uses ESTAR modeling of the Bethe stopping power of an idealized beam of REs in JET-ILW. Refs. [18, 19] use guiding center test particle modeling using KORCGC, a predecessor of KORC, with 2D axisymmetric fields and Monte Carlo collision operators having physics of bound electrons and partially-ionized impurities with constant density profiles.

Several studies using guiding center test particle modeling have also been employed to study RE generation and confinement during the thermal quench of a disruption. Refs. [20, 21] use the ANTS code to evolve particle orbits in 3D fields. Refs. [22, 23] use the RE orbit module in JOREK to calculate RE confinement and hot tail and Dreicer generation during a simulated thermal quench. Ref. [24] uses the RE orbit module in NIMROD to calculate RE confinement during impurity injection induced thermal quench and Ref. [25] uses the same module to calculate RE confinement with a pre-seeded large-scale island structure. Ref. [26] uses a RE orbit module with Monte Carlo collision operators having physics of bound electrons and partially-ionized impurities to calculate the post thermal quench spatial distribution of REs. Ref. [27] uses a RE orbit module in MARS-F to calculate RE loss by magnetohydrodynamic (MHD) instabilities. The confinement of REs in stochastic magnetic fields characteristic of the thermal quench phase was studied in Ref. [28].

Additional previous studies have developed tools for modeling the transport of injected impurities. Ref. [29] developed KPRAD to study the effect of MGI on disruptions. Ref. [30] developed the 1D radial fluid code IMAGINE to model MGI with comparisons to JET interferometer diagnostics. Ref. [31] recently developed a 1D diffusion model for impurity profiles and evolution.

The present study builds on previous research by incorporating experimentally-reconstructed, time-dependent

* corresponding author: beidlermt@ornl.gov

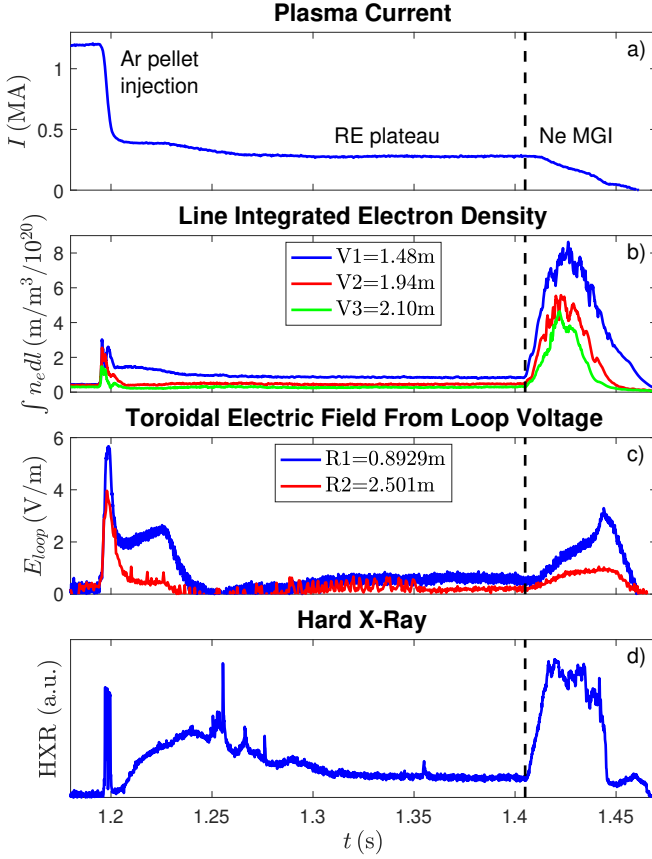


FIG. 1. DIII-D discharge #164409 with Ne MGI into the post-disruption, RE plateau, dissipating the RE current in panel a). The impurity injection results in greatly increased densities at time 1.405 ms (marked by vertical, dashed line) as seen by interferometer chord data in b). Changes in RE current after Ne MGI drive a toroidal loop voltage consistent with a toroidal electric field in panel c). REs interacting with the companion plasma and limiters produce hard x-rays in panel d).

magnetic and electric fields and employing models for the spatial-dependence of the injected impurity and electron density. Additionally, the flexible KORC framework is used to simulate RE dissipation with different models for bound electrons and partially-ionized impurity physics. We note that the physics of large-angle collisions comprising a source of secondary RE generation is not included in the present modeling, but implementation is underway for future studies. The code KORC has been extended to serve as a general framework for simulating RE physics, including validation and verification of the theoretical models needed to understand RE dissipation by impurity injection.

A major theme and contribution of the present paper is the assessment of the effectiveness of RE dissipation given the competing time scales of the RE loss of confinement (due to the displacement of the flux surfaces and the eventual loss of magnetic confinement) and RE energy dissipation. The remainder of this paper is organized as follows. In Sec. II we introduce the extensions to KORC permitting the study of RE dissipation by impurity injection, including relativistic guiding cen-

ter equations of motion, incorporating experimentally-reconstructed magnetic and toroidal electric fields, models for a spatiotemporal density profile, Monte Carlo linearized, Coulomb collision operator with models of bound electron effects, and synchrotron and bremsstrahlung radiation models. In Sec. III we discuss the initialization of the RE distributions used in KORC simulations. In Sec. IV we present results of KORC simulations and comparisons to DIII-D experiment #164409. Lastly, in Sec. V we provide concluding remarks.

II. PHYSICS MODEL

A. Relativistic Guiding-Center Equations

The original development of KORC in Ref. [13] stressed the importance of full orbit (FO) effects in RE calculations. Inclusion of FO effects enabled accurate calculation of synchrotron emission [32] and comparison with experimental observations [19]. For the present study, retaining FO effects yields calculations that are prohibitively numerically expensive. To make modeling RE orbits for the duration of the RE dissipation phase numerically feasible, we employ the relativistic guiding center (RGC) model from Refs. [33, 34]

$$\frac{d\mathbf{X}}{dt} = \frac{1}{\mathbf{b} \cdot \mathbf{B}^*} \left(e\mathbf{E} \times \mathbf{b} - p_{\parallel} \frac{\partial \mathbf{b}}{\partial t} \times \mathbf{b} + \frac{m\mu \mathbf{b} \times \nabla B + p_{\parallel} \mathbf{B}^*}{m\gamma_{gc}} \right) \quad (1a)$$

$$\frac{dp_{\parallel}}{dt} = \frac{\mathbf{B}^*}{\mathbf{b} \cdot \mathbf{B}^*} \cdot \left(e\mathbf{E} - p_{\parallel} \frac{\partial \mathbf{b}}{\partial t} - \frac{\mu \nabla B}{\gamma_{gc}} \right), \quad (1b)$$

where $\mathbf{X} \in \mathbb{R}^3$ denotes the spatial location of the GC in cylindrical (R, ϕ, Z) coordinates and $p_{\parallel} \in \mathbb{R}$ denotes the component of the relativistic momentum along the magnetic field, $p_{\parallel} \equiv \gamma m(\mathbf{V} \cdot \mathbf{b}) = \gamma mV \cos \eta$, with $\mathbf{V} = d\mathbf{X}/dt$ the velocity of the GC, $\mathbf{b} = \mathbf{B}/B$ the unit magnetic field vector, η the pitch angle, m the particle mass, e the particle charge, $\gamma = [1 - (V/c)^2]^{-1/2}$, and the magnitude of a vector \mathbf{A} given by $A = \sqrt{\mathbf{A} \cdot \mathbf{A}}$. The magnetic moment is defined as

$$\mu = \frac{|\mathbf{p} - p_{\parallel} \mathbf{b}|^2}{2mB} = \frac{p_{\perp}^2}{2mB}, \quad (2)$$

and is assumed constant in the absence of collisions and radiation, with $p_{\perp} = \gamma mV \sin \eta$. The “effective” magnetic field is defined as

$$\mathbf{B}^* = q\mathbf{B} + p_{\parallel} \nabla \times \mathbf{b}, \quad (3)$$

and the GC relativistic factor is defined as

$$\gamma_{gc} = \sqrt{1 + \left(\frac{p_{\parallel}}{mc} \right)^2 + \frac{2\mu B}{mc^2}}. \quad (4)$$

Note that the RGC model is also used in Ref. [28], where their Fig. 15 compares FO and RGC orbits. Planned

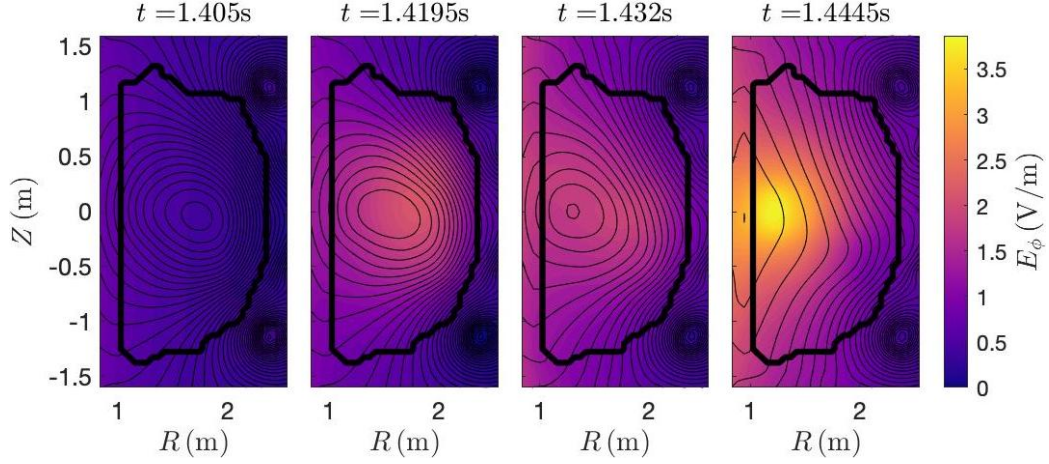


FIG. 2. Snapshots of the time-evolving, poloidal flux contours (thin, black contours) from DIII-D discharge #164409 as calculated with JFIT. The overlaid thick, black contour shows the approximate first wall of DIII-D. The colormap indicates the toroidal electric field as calculated from the time-derivative of the poloidal flux contours.

future work will utilize output from simulations using the RGC model to initialize shorter duration calculations with the FO model for evaluating synchrotron emission to be used in comparisons with experimental observations.

In the present work, we assume the static magnetic field limit of the RGC equations, by ignoring the second terms in the parenthesis of both Eqs. (1a) and (1b). This can be shown to be valid by scaling the right-hand-side (RHS) velocity terms for the spatial location

$$e\mathbf{E} \times \mathbf{b} \sim e \sim 10^{-19} \quad (5a)$$

$$p_{\parallel} \frac{\partial \mathbf{b}}{\partial t} \times \mathbf{b} \sim \gamma m_e c \sim 10^{-21} \quad (5b)$$

$$\frac{\mu}{\gamma} \mathbf{b} \times \nabla B \sim \gamma m_e c^2 \eta^2 \sim 10^{-14} \quad (5c)$$

$$\frac{p_{\parallel} \mathbf{B}^*}{m_e \gamma} \sim ec \sim 10^{-11} \quad (5d)$$

where we assume a RE has kinetic energy of 10 MeV and pitch angle of 10° , electric field, magnetic field, and spatial length scale are of order unity, and Faraday's law is used to scale $\partial \mathbf{b} / \partial t$. The term coming from the covariant relativistic correction proportional to the time-derivative of the magnetic unit vector is the smallest contribution, and many orders of magnitude smaller than the leading terms. More precise calculations (not shown) also indicate the applicability of the static magnetic field limit used in the equations of motion in this work. This limit is taken because calculating the time-derivative of the magnetic field would double the number of interpolations needed, leading to additional computational costs.

The model equations are integrated employing the Cash-Karp 5th order Runge-Kutta method [35]. For an axisymmetric magnetic configuration, in the absence of an electric-field, collisions, or radiation, energy and the canonical toroidal angular momentum are conserved. These conserved quantities are used to test the accuracy of orbit calculations in an axisymmetric magnetic configuration without electric field, collisions, or radiation. Note that the calculations in Sec. IV do not have these restrictions and energy and canonical toroidal

angular momentum are not conserved. We find that the accuracy of calculations are dependent on resolving the magnitude of magnetic curvature in the configuration, dominated by the motion parallel to the magnetic field, consistent with Eq. (5d). Based on the results of a convergence study of time step (not shown), we use $dt = eB_0 / \gamma m_e = 3.4321 \times 10^{-10}$ (s) in all simulations, calculated for a RE with kinetic energy of 10 MeV.

B. Plasma Model

The magnetic field components in the poloidal-plane are calculated from the poloidal flux function ψ_p as determined from JFIT reconstructions [36] of DIII-D discharges. The JFIT reconstruction differs from the more often used EFIT reconstruction [37], in that it doesn't find an Grad-Shafranov equilibrium, instead calculating poloidal flux from a best-fit toroidal current distribution composed of distributed-current (plasma) elements as well as passive structure currents (such as sections of the vacuum vessel), as constrained by magnetic diagnostics and measured equilibrium coil currents. In the RE plateau, due to the low temperature and density of the companion plasma, the neutral beams needed for Motional Stark Effect [38] magnetic diagnostic are not available, due to the risk of shine through and damage to the first wall. Thus, there are no internal magnetic diagnostics available for constraining the JFIT equilibrium used in this study. However, because the constraints provided by magnetic diagnostics near the edge of the plasma ensure a reliable reconstruction of the last closed flux surface, and the primary concern of this work is to assess the comparative loss of confinement and collisional dissipation of REs, JFIT reconstructions are suitable for this study.

KORC uses JFIT-computed ψ_p on a $(NR \times NZ) = (33 \times 65)$ grid, which is then interpolated using the PSPLINE cubic spline interpolation routines [39]. In the cylindrical coordinate frame (R, ϕ, Z) we adopt the convention $\mathbf{B}_p = \nabla \phi \times \nabla \psi_p$ for the poloidal

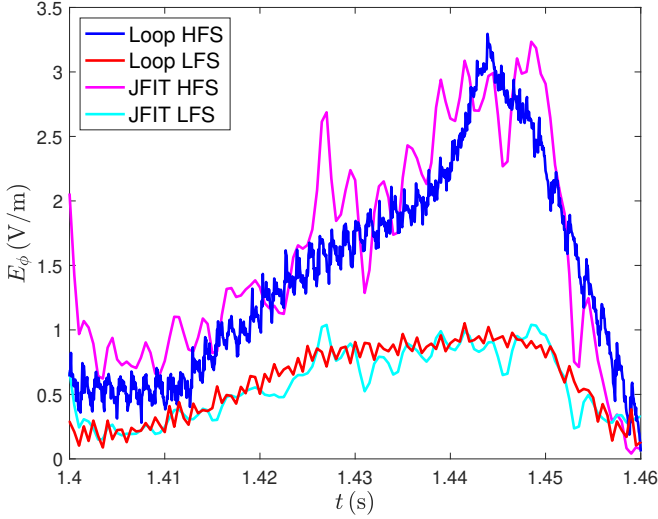


FIG. 3. Measurements of the toroidal electric field calculated via the toroidal loop voltage for DIII-D experiment #164409 at the HFS $R = 0.8929$ (m) (dark, blue trace) and the LFS $R = 2.5010$ (m) (red trace). Point measurements of the toroidal electric field calculated via time-derivatives of the JFIT poloidal flux function are shown at the HFS (violet trace) and LFS (cyan trace).

field components yielding $B_R = (1/R)\partial\psi_p/\partial Z$, $B_Z = -(1/R)\partial\psi_p/\partial R$, where the gradients are computed using the spline representation in PSPLINE. In the discharges of interest the current is directed in the positive ϕ direction, giving ψ_p a local minimum at the magnetic axis. The toroidal magnetic field component is calculated assuming $B_\phi = -R_0 B_0 / R$, directed in the counter- I_p direction, where $R_0 = 1.682$ m and $B_0 = 2.141$ T are the major radial location and toroidal field near the magnetic axis for DIII-D discharge #164409. This model for the toroidal magnetic field does not include the self-consistent correction due to poloidal RE motion, however simple calculations (not shown) indicate that this correction should be on the order of 0.1%. In addition to calculating the magnetic field components by taking the first derivatives using the PSPLINE routines, we also calculate the second order derivatives from the spline representation of ψ_p to compute the ∇B and $\nabla \times \mathbf{b}$ “auxiliary” fields needed to integrate Eqs. (1a-1b).

In this work, we use time-sequenced JFIT reconstructions of ψ_p that are spaced 0.5 ms apart. We preprocess this data with MATLAB, first smoothing ψ_p over 5 ms intervals, and then taking the time-derivative using a central difference method to calculate E_ϕ according to $E_\phi = (1/2\pi R)\partial\psi_p/\partial t$. Snapshots of the smoothed ψ_p contours are shown in Fig. 2, by the thin contours, where the thick contour indicates the DIII-D first wall. The experimentally inferred magnetic fields are by construction axisymmetric and thus they are not stochastic. Although exploring the potential role of magnetic field stochasticity is outside the scope of the present paper, we believe that in this case this effect is much less important than the fast deconfinement due to the scrap off. It is also important to keep in mind that in some regimes the deconfinement of RE due to magnetic stochasticity is less

than commonly thought, see for example Ref. [28]. As the current decays, Fig. 2 indicates that flux surfaces advect toward the inner wall limiter. At present, there are two possibilities for this advection: ineffectiveness of the position controller at low currents [40], or evolution of canonical toroidal angular momentum as REs decelerate [41]. It is outside of the scope of this work to determine the cause of this advection, but rather analyze the consequences for RE confinement and collisional dissipation. The calculated toroidal electric field is shown in Fig. 2 by the colormap. To check the robustness of the method for calculating E_ϕ , we compare values calculated from the JFIT reconstructions with data from loop voltages measurements from the HFS and LFS of DIII-D in Fig. 3, which indicates good agreement. At the beginning of each simulation and 5 ms intervals thereafter, PSPLINE recalculates the interpolants for ψ_p and E_ϕ for the next time interval.

The electron temperature of the plasma is assumed temporally and spatially constant at $T_e = 1.5$ eV as seen from Thomson scattering measurements taken before impurity injection (not shown), which is also consistent with fits to line emission brightness in Ref. [11]. The effective impurity nuclear charge is also assumed temporally and spatially constant at $Z_{\text{eff}} = 1$. We will comment how these assumptions will affect modeling in Secs. II C 2, II C 3. The electron density takes the form of a temporally and spatially evolving, constricting “ring” profile. This profile is given by that of a Gaussian centered at a chosen flux surface with a time-dependent magnitude and width parameterized as

$$n_e(\psi_p, t) = \frac{n_r - n_0}{2} \left[\tanh\left(\frac{t - \tau_{\text{in}}}{\tau_{\text{in}}}\right) - \tanh\left(\frac{t - t_{\text{delay}}}{\tau_{\text{out}}}\right) \right] \times \exp\left[-\frac{(\sqrt{\psi_p} - \sqrt{\psi_{p,0}})^2}{2\sigma_{\psi_p}^2(t)}\right] \quad (6a)$$

$$\sigma_{\psi_p}(t) = \lambda_n \operatorname{erf}\left(\frac{t}{\tau_n}\right) \quad (6b)$$

where n_r is the maximum density of the profile, n_0 is the background density, τ_{in} , τ_{out} , and t_{delay} parameterize the time scale over which the density increases, decreases, and remains constant, respectively, $\psi_{p,0}$ the poloidal flux surface where the Gaussian is centered, λ_n is the maximum width of the Gaussian, and τ_n is the time scale over which the Gaussian width increases.

Physically, as impurities are injected via SPI, they first encounter a cold companion plasma, with little ionization of the impurities. As the impurities reach the RE beam, the impurities are rapidly ionized and the resulting electrons move along poloidal flux surfaces. This ring structure can be seen experimentally by visible cameras (not shown). Due to the low temperatures of the companion plasma, the electrons and impurities diffuse across magnetic surfaces [11]. Lastly, as the current decreases, the electrons and impurities are deconfined due to the motion of the flux surfaces.

This work assumes that all impurity charge states considered have the same spatiotemporal profile as n_e , with only changes in their ratio n_j/n_e . Presently we assume

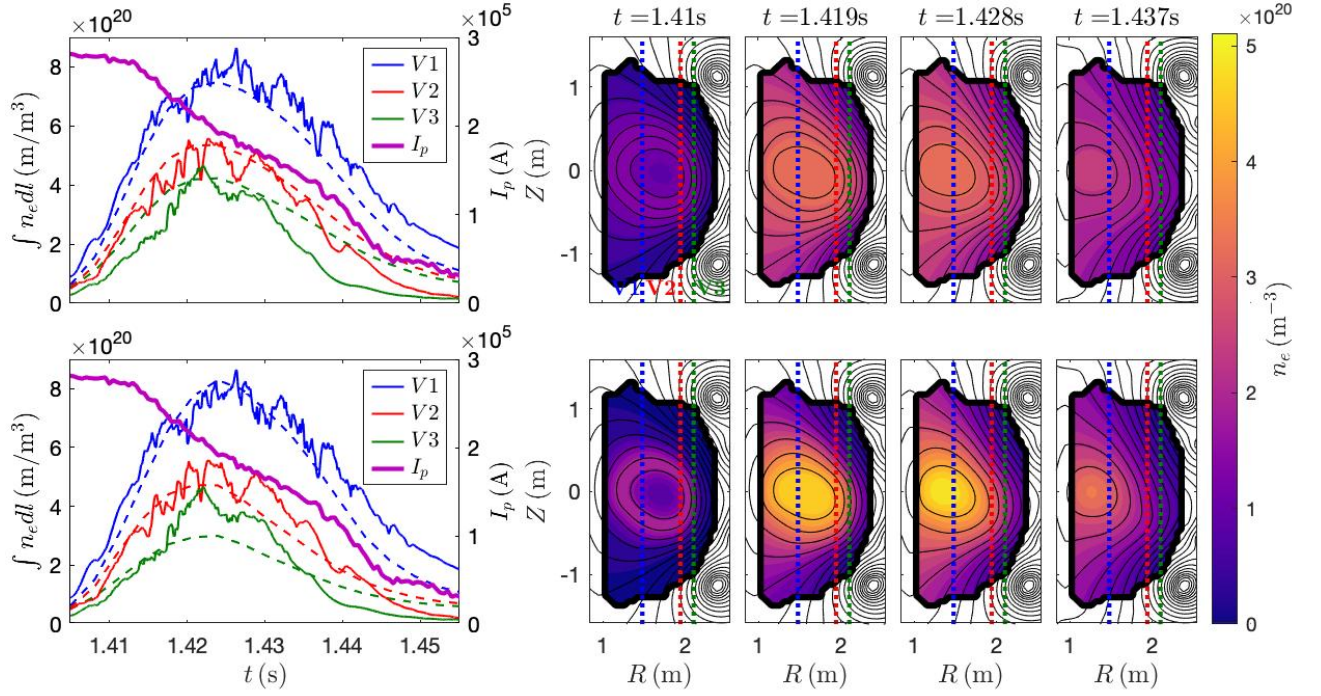


FIG. 4. Left plots show experimental current and line integrated density measurements in solid traces for DIII-D discharge #164409. Dashed traces indicate synthetic interferometer diagnostic results using the spatiotemporal density profile from Eqs. (6a)-(6b), where the top plot uses a broad and diffuse profile with parameters in the top row of Table I and the bottom plot uses a narrow and dense profile with parameters from the bottom row. Right plots show spatiotemporal density profiles at different time slices, where the vertical dashed lines indicate the location of the interferometer diagnostics on DIII-D. Note that the different spatiotemporal profiles record similar synthetic interferometer signals.

n_r (m^{-3})	n_0 (m^{-3})	τ_{in} (s)	τ_{out} (s)	t_{delay} (s)	$\psi_{p,0}$	λ_n	τ_n (s)
4×10^{20}	2.5×10^{19}	7.5×10^{-3}	1.25×10^{-2}	4×10^{-2}	0.8	0.255	1.5×10^{-2}
7×10^{20}	2.5×10^{19}	10^{-2}	1.25×10^{-2}	5×10^{-2}	0.775	0.15	1.75×10^{-2}

TABLE I. Spatiotemporal density profile fitting parameters for modeling DIII-D discharge #164409. Top row corresponds the a broad and diffuse profile while the bottom row corresponds to a narrow and dense profile.

the companion plasma contains two partially-ionized impurity charge states, with $n_{Ne+1}/n_{Ne+2} = 2$. This choice of impurity composition is roughly in line with results presented in Ref. [31]. While the companion plasma contains a significant D+ population in the pre-MGI state, Ref. [31] infers that D+ plays an insignificant role in the post-MGI state studied in this work.”

We will further discuss the calculation of impurity charge state densities and the affect of the assumed charge state ratio in Sec. II C 3.

In the following simulations, two spatiotemporal profiles are used, a “broad and diffuse” profile, seen in the top row of plots in Fig. 4 with parameters in the top row of Table I, and a “narrow and dense” profile seen in the bottom row of plots in Fig. 4 with parameters in the bottom row of Table I. The left column of plots in Fig. 4 compare line-integrated electron density interferometer diagnostic data from DIII-D discharge #164409 with synthetic line-integrated density diagnostic applied to the model density shown in the right plots of Fig. 4. The two spatiotemporal density profiles were chosen to test

the sensitivity of the model used given the line-integrated measurements.

C. Coulomb Collisions

1. Monte Carlo Operator

In flux-conserving form, the Fokker-Planck partial differential equation (PDE) with a Coulomb collision operator in azimuthally-symmetric spherical momentum space (*e.g.* [42])

$$\mathcal{C}(f) = \frac{1}{p^2} \frac{\partial}{\partial p} \left[p^2 \left(C_A \frac{\partial f}{\partial p} + C_F f \right) \right] + \frac{C_B}{p^2} \left[\frac{1}{\sin \eta} \frac{\partial}{\partial \eta} \left(\sin \eta \frac{\partial f}{\partial \eta} \right) \right] \quad (7)$$

can be written [43] as two equivalent stochastic differential equations (SDEs) for the phase-space momentum,

given by

$$dp = \left\{ -C_F(p) + \frac{1}{p^2} \frac{\partial}{\partial p} [p^2 C_A(p)] \right\} dt + \sqrt{2C_A(p)} dW_p, \quad (8a)$$

$$d\eta = \frac{C_B(p)}{p^2} \cot \eta dt + \frac{\sqrt{2C_B(p)}}{p} dW_\eta, \quad (8b)$$

where C_F , C_A , and C_B are linearized transport coefficients for collisional friction (slowing down), parallel diffusion, and pitch angle scattering (deflection), respectively, and dW is a zero mean, unit standard deviation Weiner process satisfying

$$\langle dW \rangle = 0, \quad \langle (dW)^2 \rangle = dt. \quad (9)$$

Here, we use uniformly-distributed random numbers, which behave better than normally-distributed random numbers at low energies, due to their tighter bounds. Applying Itô's lemma [43] by letting $\xi = \cos \eta$ yields

$$d\xi = -2\xi \frac{C_B(p)}{p^2} dt - \frac{\sqrt{2C_B(p)}}{p} \sqrt{1 - \xi^2} dW_\xi. \quad (10)$$

The Coulomb collision operator SDEs are subcycled independently of the RGC equations of motion using an operator splitting method. The time step of the collision operator is set as the 1/20 of the shortest inverse collision frequency (to be defined in the following subsections). While this temporal resolution accurately captures the damping of relativistic particles, with relatively long inverse collision frequencies, once particles thermalize this temporal resolution is not sufficient, consistent with the divergence of $d\eta$ as $p \rightarrow 0$. Thus, for this study, when a particle's momentum satisfies $p < m_e c$, the particle is flagged as thermalized and is not tracked anymore. Future studies, especially for the generation of runaways from a thermal plasma following the thermal quench, will require a significant increase in the collision substep cadence. Additionally, we again mention that the physics of large-angle collisions comprising a source of secondary RE generation is not included in the present modeling, and its implementation is expected to increase the collision subcycling frequency substantially.

2. Relativistic Transport Coefficients

In the absence of bound electron and partially-ionized impurity physics, Ref. [20] generalizes the collision operator coefficients C_A , C_F , C_B to combine the non-relativistic [42] and relativistic [44] energy limits, yielding

$$C_A(v) = \frac{\Gamma_{ee} \mathcal{G}\left(\frac{v}{v_{th}}\right)}{v}, \quad (11a)$$

$$C_F(v) = \frac{\Gamma_{ee} \mathcal{G}\left(\frac{v}{v_{th}}\right)}{T_e}, \quad (11b)$$

$$C_B(v) = \frac{\Gamma_{ei}}{2v} Z_{eff} + \frac{\Gamma_{ee}}{2v} \left[\text{erf}\left(\frac{v}{v_{th}}\right) - \mathcal{G}\left(\frac{v}{v_{th}}\right) + \frac{1}{2} \left(\frac{v_{th} v}{c^2}\right)^2 \right], \quad (11c)$$

where $\Gamma_{ee,ei} = n_e e^4 \ln \Lambda_{ee,ei} / 4\pi \epsilon_0^2$ with $\ln \Lambda_{ee,ei}$ the Coulomb logarithm for e-e(e-i) collisions, $v_{th} = \sqrt{2T_e/m_e}$ the thermal electron velocity,

$$\mathcal{G}(x) = \frac{\text{erf}(x) - x \text{erf}'(x)}{2x^2} \quad (12)$$

is the Chandrasekhar function, where the prime indicates a derivative with respect to the independent variable. The expressions for $\ln \Lambda_{ee,ei}$ are taken from Ref. [7]

$$\ln \Lambda_{ee} = \ln \Lambda_0 + \frac{1}{5} \ln \left\{ 1 + [2(\gamma - 1)c^2/v_{th}^2]^{5/2} \right\} \quad (13a)$$

$$\ln \Lambda_{ei} = \ln \Lambda_0 + \frac{1}{5} \ln \left[1 + (2\gamma v/v_{th})^5 \right] \quad (13b)$$

$$\ln \Lambda_0 = 14.9 - \frac{\ln n_e (10^{20} \text{ m}^{-3})}{2} + \ln T(\text{keV}). \quad (13c)$$

Note that the term in Eq. (11c) proportional to Z_{eff} is taken from relativistic collision theory, and this term diverges as $v \rightarrow 0$. For a 10 MeV RE, changing T_e of the companion plasma by a factor of 10 yields a 6% difference in $\ln \Lambda_{ei}$, a 7% difference in $\ln \Lambda_{ee}$, and factor of 10 change to \mathcal{G} . However, in C_F , the change in \mathcal{G} is offset by the change in T_e , and in C_B , \mathcal{G} is small compared to the first term in the brackets, leading to a low sensitivity of collisions on T_e for REs. Conversely, C_B scales nearly as $(Z_{eff} + 1)$, so changes in Z_{eff} are strongly felt in the pitch angle scattering in the absence of bound electrons.

Using the relation $dp = m_e \gamma^3 dv$, the second term in the brackets of Eq. (8a) can be evaluated as

$$\frac{1}{p^2} \frac{\partial}{\partial p} [p^2 C_A(p)] = \frac{\Gamma_{ee}}{\gamma^3 m_e v^2} \left\{ \left[2\gamma^2 \left(\frac{v}{c}\right)^2 - 1 \right] \mathcal{G}\left(\frac{v}{v_{th}}\right) + \frac{v}{v_{th}} \text{erf}'\left(\frac{v}{v_{th}}\right) \right\}. \quad (14)$$

Note, that this form does not treat the momentum dependence in the Coulomb logarithm.

3. Bound Electrons

The transport coefficients given in Eqs. (11a-11c) describe normalized collision frequencies due to Coulomb

collisions with ions and free electrons according to

$$C_A(v) \equiv \frac{p^2}{2} \nu_{\parallel}^{ee}, \quad (15a)$$

$$C_F(v) \equiv p \nu_S^{ee}, \quad (15b)$$

$$C_B(v) \equiv \frac{p^2}{2} (\nu_D^{ei} + \nu_D^{ee}), \quad (15c)$$

where the factor of 1/2 used in Ref. [42] for the definition of Eq. (15b) has been absorbed into ν_S^{ee} as done in Ref. [7]. However the bound electrons of the partially ionized impurities will also play an important role. Reference [7] considers the effects of bound electrons on the slowing down e-e collision frequency by including a multiplicative factor according to Bethe's theory for collisional stopping power [45]

$$\nu_S^{ee} = \nu_{S,CS}^{ee} \left\{ 1 + \sum_j \frac{n_j}{n_e} \frac{Z_j - Z_{0j}}{\ln \Lambda} \left[\frac{1}{5} \ln(1 + h_j^5) - \beta^2 \right] \right\}, \quad (16)$$

where $\nu_{S,CS}^{ee}$ is the “completely screened” slowing down frequency consistent with the models neglecting bound electron physics given by Eqs. (15b,11b), the sum is over the ionization state, n_j is the density of the j -th ionization state, Z_j is the unscreened (*i.e.* fully ionized) impurity ion charge, Z_{0j} is the screened (*i.e.* partially ionized) impurity ion charge, $h_j = p\sqrt{\gamma - 1}/(m_e c I_j)$, where I_j is the mean excitation energy provided in Ref. [46], and $\beta = v/c$ is the usual relativistic speed. The factor $Z_j - Z_{0j}$ is recognized as the number of bound electrons a partially-ionized impurity charge state possesses. The following simulations assume that all impurity charge states considered have the same spatiotemporal profile as n_e , with only changes their ratio n_j/n_e satisfying

$$n_e = \sum_j k_j n_j, \quad (17)$$

where k_j is the charge state for a particular partially-ionized impurity j .

The effects of bound electrons on the pitch-angle diffusion e-i collision frequency is considered using the Born approximation [47, 48] to yield the modification

$$\nu_D^{ei} = \nu_{D,CS}^{ei} \left(1 + \frac{1}{Z_{\text{eff}}} \sum_j \frac{n_j}{n_e} \frac{g_j}{\ln \Lambda_{ei}} \right), \quad (18)$$

where $\nu_{D,CS}^{ei}$ is the completely screened pitch angle scattering frequency consistent with the models neglecting bound electron physics given by Eq. (15c) and the first term of Eq. (11c),

$$g_j = \frac{2}{3} (Z_j^2 - Z_{0j}^2) \ln(y_j^{3/2} + 1) - \frac{2}{3} \frac{(Z_j - Z_{0j})^2 y_j^{3/2}}{y_j^{3/2} + 1} \quad (19)$$

with $y_j = p \bar{a}_j / (m_e c)$, and \bar{a}_j is the normalized effective ion scale length for impurity charge state j . The values of \bar{a}_j are determined from the density of bound electrons as calculated in Ref. [8]. For a 10 MeV RE and a companion

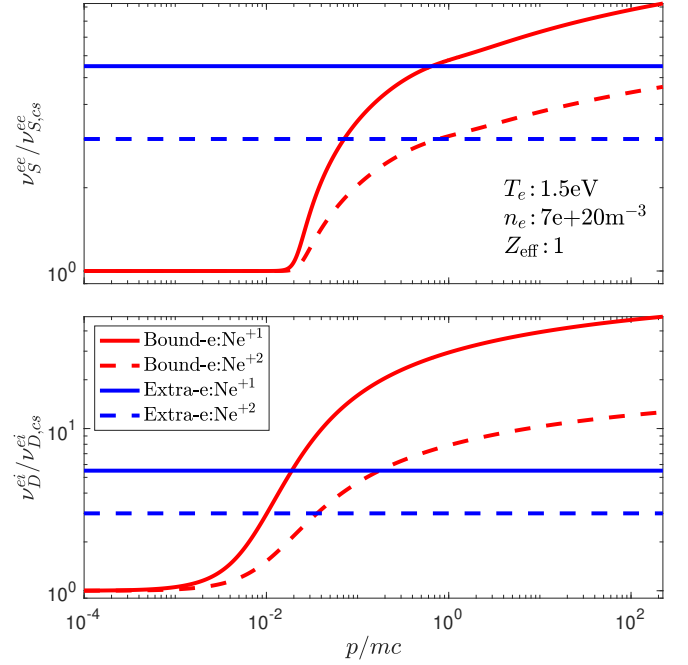


FIG. 5. Top plot shows the slowing down collision frequency with the inclusion of bound electrons normalized to the frequency without bound electron physics. Bottom plot shows the pitch angle diffusion collision frequency with the inclusion of bound electrons normalized to the frequency without bound electron physics. Red traces indicate the Bound-e model and blue traces indicate the Extra-e model. Solid traces are for Ne^{+1} and dashed traces for Ne^{+2} .

plasma with $n_{\text{Ne}^{+1}}/n_{\text{Ne}^{+2}} = 2$, the ratio between the Z_{eff} and bound electron contributions to ν_D^{ei} is roughly 1.5 : 22.5. If the addition of Ar impurities from the initially injected pellet were included, this ratio would most likely narrow, but still have the bound electron contribution outweigh the Z_{eff} contribution to pitch angle scattering. Future modeling should better account for more realistic partially-ionized impurity species.

With the model in Ref. [8] of bound electrons and partially-ionized impurities, the transport coefficients become

$$C_{A,\text{Bound}}(v) = \frac{\Gamma_{ee} \mathcal{G}(\frac{v}{v_{\text{th}}})}{v}, \quad (20a)$$

$$C_{F,\text{Bound}}(v) = \frac{\Gamma_{ee} \mathcal{G}(\frac{v}{v_{\text{th}}})}{T_e} \left\{ 1 + \sum_j \frac{n_j}{n_e} \frac{Z_j - Z_{0j}}{\ln \Lambda_{ee}} \times \left[\frac{1}{5} \ln(1 + h_j^5) - \beta^2 \right] \right\}, \quad (20b)$$

$$C_{B,\text{Bound}}(v) = \frac{\Gamma_{ei}}{2v} Z_{\text{eff}} \left(1 + \frac{1}{Z_{\text{eff}}} \sum_j \frac{n_j}{n_e} \frac{g_j}{\ln \Lambda_{ei}} \right) + \frac{\Gamma_{ee}}{2v} \left[\text{erf} \left(\frac{v}{v_{\text{th}}} \right) - \mathcal{G} \left(\frac{v}{v_{\text{th}}} \right) + \frac{1}{2} \left(\frac{v_{\text{th}} v}{c^2} \right)^2 \right]. \quad (20c)$$

Reference [7] also pointed to comments in Ref. [49] about the inclusion of bound electrons in avalanche phe-

nomena. Reference [7] incorporated these comments by modifying the slowing down e-e collision frequency to include half of the bound electrons

$$\nu_S^{ee} = \nu_{S,CS}^{ee} \left(1 + \sum_j \frac{n_j}{n_e} \frac{Z_j - Z_{0j}}{2} \right). \quad (21)$$

Note that bound electrons in Eq. 21 are treated the same as free electrons when it comes to their effect on the collision frequency, as compared with Eq. 16 that treats bound electrons according to Bethe's theory for collisional stopping power. We have also incorporated similar modifications to the pitch-angle diffusion e-i collision frequency

$$\nu_D^{ei} = \nu_{D,CS}^{ei} \left(1 + \sum_j \frac{n_j}{n_e} \frac{Z_j - Z_{0j}}{2} \right). \quad (22)$$

Note that this modification only makes sense for the assumption $Z_{\text{eff}} = 1$ being used in the present study. With the model of bound electrons and partially-ionized impurities according to Ref. [49], the transport coefficients become

$$C_{A,\text{Extra}}(v) = \frac{\Gamma_{ee} \mathcal{G}(\frac{v}{v_{\text{th}}})}{v}, \quad (23a)$$

$$C_{F,\text{Extra}}(v) = \frac{\Gamma_{ee} \mathcal{G}(\frac{v}{v_{\text{th}}})}{T_e} \left(1 + \sum_j \frac{n_j}{n_e} \frac{Z_j - Z_{0j}}{2} \right), \quad (23b)$$

$$C_{B,\text{Extra}}(v) = \frac{\Gamma_{ei}}{2v} Z_{\text{eff}} \left(1 + \sum_j \frac{n_j}{n_e} \frac{Z_j - Z_{0j}}{2} \right) + \frac{\Gamma_{ee}}{2v} \left[\text{erf} \left(\frac{v}{v_{\text{th}}} \right) - \mathcal{G} \left(\frac{v}{v_{\text{th}}} \right) + \frac{1}{2} \left(\frac{v_{\text{th}} v}{c^2} \right)^2 \right]. \quad (23c)$$

In the following simulations, we will refer to 3 collision models, “No-Bound” with transport coefficients given by Eqs. (11a-11c) with no bound electrons, “Bound-e” with transport coefficients given by Eqs. (20a-20c), and “Extra-e” with transport coefficient given by Eqs. (23a-23c). Figure 5 shows the slowing down frequency in the top plot and the pitch angle scattering frequency in the bottom plot for singly-ionized Ar and Ne using the Bound-e and Extra-e models. The collision frequencies are normalized to the completely screened, or No-Bound, collision frequencies.

D. Radiation Damping

Simulations also include the effects of synchrotron radiation due to the radiation reaction force \mathbf{F}_R . The Landau-Lifshitz representation [50] of the Lorentz-Abraham-Dirac radiation reaction force, ignoring the electric field and advective derivatives, is

$$\mathbf{F}_R = \frac{1}{\gamma \tau_R} \left[(\mathbf{p} \times \mathbf{b}) \times \mathbf{b} - \frac{1}{(m_e c)^2} (\mathbf{p} \times \mathbf{b})^2 \mathbf{p} \right], \quad (24)$$

where $\tau_R = 6\pi\epsilon_0(m_e c)^3/(e^4 B^2)$ is the radiation damping time scale. In azimuthally-symmetric spherical momentum space, with the identity $(\hat{\mathbf{p}} \times \mathbf{b}) \times \mathbf{b} = -\sin \eta \hat{\mathbf{p}} - \cos \eta \hat{\eta}$, the flux-conserving form of the Fokker-Planck PDE can be written as two equivalent SDEs given by

$$\frac{dp}{dt} = -\frac{\gamma p}{\tau_R} (1 - \xi^2) \quad (25a)$$

$$\frac{d\xi}{dt} = \frac{\xi(1 - \xi^2)}{\tau_R \gamma}. \quad (25b)$$

Equation (25a) is consistent with the relativistic Larmor formula (e.g. [51]).

The evolution equations for (p, ξ) in Eqs. (25a-25b) can be transformed into evolution equations for (p_{\parallel}, μ) yielding

$$\frac{dp_{\parallel}}{dt} = -\frac{p_{\parallel}(1 - \xi^2)}{\tau_R} \left(\gamma - \frac{1}{\gamma} \right) \quad (26a)$$

$$\frac{d\mu}{dt} = -\frac{2\mu}{\tau_R} \left[\gamma(1 - \xi^2) + \frac{\xi^2}{\gamma} \right]. \quad (26b)$$

These deterministic evolution equations are added to the Cash-Karp algorithm for integrating the GC equations of motion by adding the RHS of Eq. (26a) to the RHS of Eq. (1b) and using Eq. (26b) to evolve the magnetic moment. We note that Eq. (24) is to be taken at the location of a moving charge, so the above implementation is only valid for a small gyroradius. A specific formulation for the GC equations of motion is given by Ref. [52] and will be explored in future studies.

The bremsstrahlung radiation due to runaway electrons interacting with impurities modeled as a stopping power is discussed in Ref. [53] and can be written as

$$\begin{aligned} \frac{d}{dt} [(\gamma - 1)m_e c^2] &= -2vn_j \kappa Z_{0j} (Z_{0j} + 1) \\ &\times \frac{\alpha}{\pi} (\gamma - 1) \left[\ln(2\gamma) - \frac{1}{3} \right], \end{aligned} \quad (27)$$

where $\kappa = 2\pi r_e^2 m_e c^2$, $r_e = e^2/4\pi\epsilon_0 m_e c^2$ is the classical electron radius, and $\alpha = 1/137$ is the fine structure constant. Because only the energy changes, and not the pitch angle, using $d\gamma/dp = v/(m_e c^2)$ we can write

$$\begin{aligned} \frac{dp}{dt} &= -2n_j \kappa Z_{0j} (Z_{0j} + 1) \\ &\times \frac{\alpha}{\pi} (\gamma - 1) \left[\ln(2\gamma) - \frac{1}{3} \right] \end{aligned} \quad (28a)$$

$$\frac{d\xi}{dt} = 0. \quad (28b)$$

Similarly as for synchrotron radiation, the evolution equations for (p, ξ) can be transformed into evolution

equations for (p_{\parallel}, μ) yielding

$$\frac{dp_{\parallel}}{dt} = -\xi 2n_j \kappa Z_{0j} (Z_{0j} + 1) \times \frac{\alpha}{\pi} (\gamma - 1) \left[\ln(2\gamma) - \frac{1}{3} \right] \quad (29a)$$

$$\frac{d\mu}{dt} = -\frac{(1 - \xi^2)p}{m_e B} 2n_j \kappa Z_{0j} (Z_{0j} + 1) \times \frac{\alpha}{\pi} (\gamma - 1) \left[\ln(2\gamma) - \frac{1}{3} \right]. \quad (29b)$$

These deterministic evolution equations are also added to the Cash-Karp algorithm for integrating the GC equations of motion by adding the RHS of Eq. (29a) to the RHS of Eq. (1b) and adding the RHS of Eq. (29b) to the RHS of Eq. (26b). We note that Ref. [54] formulates a Boltzmann collision operator for bremsstrahlung radiation that results in a more accurate momentum-space evolution compared to stopping power models. However, for the present study concerning RE current dissipation, the precise details of momentum phase space evolution are of lesser importance.

III. ENSEMBLE INITIALIZATION

A Metropolis-Hastings (MH) algorithm [55, 56] is employed to sample user-provided, multidimensional distribution functions using Markov-chains of Gaussian processes in each dimension. The “acceptance ratio” is calculated for every sample of the Markov-chains, comparing the new sample to the previous sample. If this ratio is greater than 1 or a uniformly-distributed random number, the new sample is accepted. Included in the acceptance ratio is the Jacobian determinant of the cylindrical spatial coordinate system R and the spherical momentum phase space $p^2 \sin \eta$. One benefit of the MH algorithm is that it only depends on the ratio of the distribution function at different sampling points, and not the absolute values, thus no normalizations are needed.

For the following simulations, we use an initial distribution of the form

$$f[R, Z, \mathcal{E}, \eta] = f_{\psi_p}[\psi_p(R, Z)] f_{\mathcal{E}}(\mathcal{E}) f_{\eta}(R, \mathcal{E}, \eta), \quad (30)$$

where $\mathcal{E} = \gamma m_e c^2$ is the total energy of a RE. Across all simulations to be presented, we assume that the initial spatial distribution has a Gaussian dependence of the form

$$f_{\psi_p}(R, Z) = \exp \left[-\frac{\psi_N(R, Z)}{\sigma_{\psi_N}} \right], \quad (31)$$

where $\psi_N = [\psi_p(R, Z) - \psi_{p,\text{axis}}] / (\psi_{p,\text{lim}} - \psi_{p,\text{axis}})$ is the normalized poloidal flux, with $\psi_{p,\text{axis}} = 0.600$ Wb the initial poloidal flux at the magnetic axis and $\psi_{p,\text{lim}} = 0.845$ Wb is the initial poloidal flux at the HFS limiter. Note that this parameterization is chosen because we desire a spatial distribution as a function of minor radius r , and $\psi \propto r^2$. A uniform distribution can be recovered by choosing σ_{ψ_N} arbitrarily large, *e.g.* $\sigma_{\psi_N} = 10^6$, and

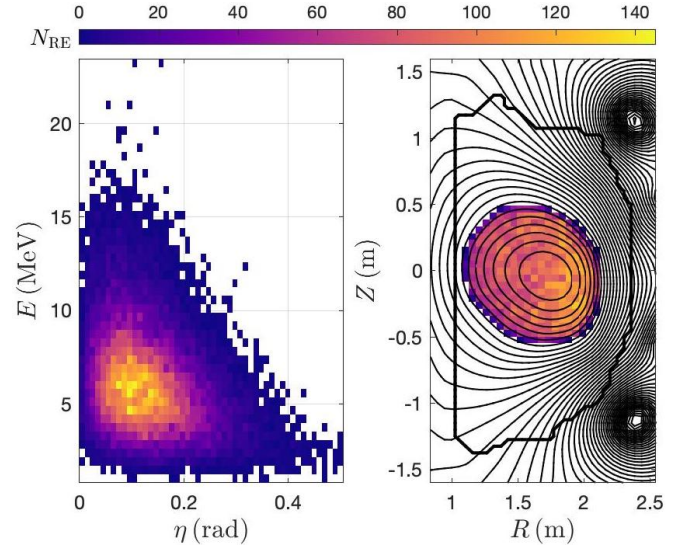


FIG. 6. Example initial distribution used for simulations of DIII-D discharge #164409 with Ne MGI with 2.5×10^4 sampled particles. E, η distribution shown in a), and R, Z distribution shown in b), with overlaid (thin) contours of ψ_p and (thick) first wall.

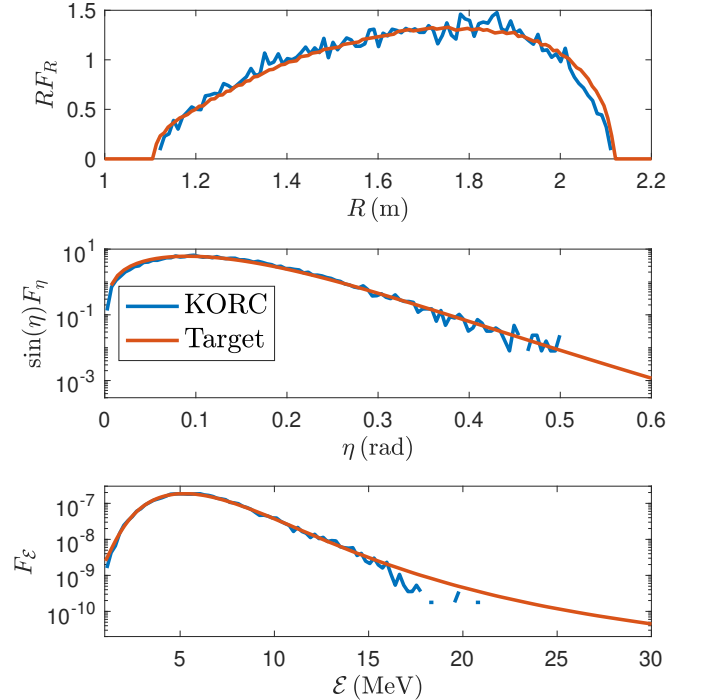


FIG. 7. Comparison between the target distribution (red traces) compared to the sampled distribution (blue traces) for a given KORC calculation. The top plot shows the spatial distribution for a uniform density of REs for DIII-D discharge #164409. The middle plot shows the pitch angle distribution given by Eqs. 32,33. The bottom plot shows the energy distribution for sampling of the distribution function inferred from a separate DIII-D discharge reported in Ref. [57].

an indicator function is used to limit sampling to where $\psi_N < 0.845$. The particles are sampled uniformly in toroidal angle ϕ . For $f_{\mathcal{E}}(\mathcal{E})$ we use either a monoenergetic distribution of 10 MeV or the distribution inferred from experimental data of a post-disruption, RE beam in Ref. [57]. For the pitch angle distribution we use either a monopitch distribution of 10° or that considered in Ref. [57], which assumes a balance between pitch angle scattering and electric field “pinching”

$$f_{\eta}(R, \mathcal{E}, \eta) = \frac{A(R, \mathcal{E})}{2 \sinh A(R, \mathcal{E})} e^{A(R, \mathcal{E})\eta}, \quad (32)$$

with

$$A(R, \mathcal{E}) = \frac{2\tilde{E}_{\phi}(R) \gamma^2 - 1}{Z_{\text{eff}} + 1 - \gamma}, \quad (33)$$

where $\tilde{E}_{\phi}(R) = E_0 R_0 / (E_{\text{CH}} R)$ is the normalized, initial, toroidal electric field, with the Connor-Hastie field [58] $E_{\text{CH}} = n_e e^3 \ln \Lambda_0 / 4\pi \epsilon_0^2 m_e c^2$, magnitude $E_0 / E_{\text{CH}} = 24.56$, and $Z_{\text{eff}} = 1$ is effective impurity nuclear charge.

For the energy and pitch angle distribution from Fig. 5 Ref. [57], the resulting distribution function is shown in Fig. 6 as a function of a) E, η and b) R, Z for 2.5×10^4 particles. Note that Fig. 6b) has overlaid (thin line) contours of ψ_p , consistent with the initial time in Sec. II B, and indicates the (thick line) approximate first wall on DIII-D. The apparent increase in the number of REs as R increases reflects the Jacobian determinant of the cylindrical coordinate system appearing when we integrate over the ϕ direction to show the distribution in the R, Z plane.

A comparison between the target distribution and sampled distribution is presented in Fig. 7. The top plot shows the distribution $F_R = \int f_{\psi_p} dZ$, where the factor of R is the Jacobian determinant of the cylindrical coordinate system used for the spatial representation. The middle plot shows the distribution $F_{\eta} = \int dZ \int R dR \int d\mathcal{E} f$, where the factor of $\sin(\eta)$ comes from the Jacobian determinant of the spherical coordinate system used for the momentum representation. And lastly the bottom plot shows the distribution $F_{\mathcal{E}} = f_{\mathcal{E}}$ reported in Ref. [57]. Note that because the target $F_{\mathcal{E}}$ decreases algebraically, rather than exponentially, the Gaussian process MH algorithm has difficulties sampling the high energy tail. However, since the majority of the RE beam energy is contained in the bulk around 6.5 MeV, this sampling is acceptable for the present modeling.

IV. RESULTS

To characterize the evolution of the ensemble of particles at a macroscopic level, we define the total RE energy \mathcal{E}_{RE}

$$\mathcal{E}_{\text{RE}}(t) = m_e c^2 \sum_i^{N_p} \gamma_i(t) \mathcal{H}_{\text{RE},i}(t) \quad (34)$$

where

$$\mathcal{H}_{\text{RE},i}(t) = \begin{cases} 1 & \text{if } p_i(t) > m_e c \\ 0 & \text{if } p_i(t) < m_e c \text{ or hits wall.} \end{cases}$$

Simulation	Collisions	Bound model	E_{ϕ}	ST model	$f(\mathcal{E}, \eta)$
Case 1	F	NA	T	NA	mono- \mathcal{E}, η
Case 2	F	NA	F	NA	mono- \mathcal{E}, η
Case 3	T	Bound-e	T	diffuse	mono- \mathcal{E}, η
Case 4	T	Extra-e	T	diffuse	mono- \mathcal{E}, η
Case 5	T	No-bound	T	diffuse	mono- \mathcal{E}, η
Case 6	T	Bound-e	T	diffuse	Ref. [57]
Case 7	T	Bound-e	T	dense	mono- \mathcal{E}, η
Case 8	T	Bound-e	T	dense	Ref. [57]

TABLE II. Models used in simulations shown in this section. ‘F/T’ are abbreviations for false/true.

\mathcal{H}_{RE} effectively splits the ensemble of particles into two populations, confined and thermalized or deconfined electrons. Note that this definition is consistent with the discussion at the end of Sec. II C, and roughly consistent with the definition of critical momentum in Ref. [49]. We also define the RE current I_{RE} , beginning from the toroidal current density $J_{\phi} = -en_e \mathbf{v} \cdot \hat{\phi}$, satisfying $I_{\text{RE}} = \int dR \int dZ J_{\phi}$. Using the definition of the density of an ensemble of particles $n_e(\mathbf{x}) = \sum_i \delta^3(\mathbf{x} - \mathbf{x}_i) = \sum_i \delta(R - R_i) \delta(Z - Z_i) / (2\pi R)$ and assuming that the toroidal component of the velocity is, to lowest order, $\mathbf{v} \cdot \hat{\phi} \simeq v_{\parallel} \mathbf{b} \cdot \hat{\phi} = v \xi b_{\phi}$ yields

$$I_{\text{RE}}(t) = -\frac{e}{2\pi} \sum_i^{N_p} \frac{v_i \xi_i b_{\phi,i}}{R_i} \mathcal{H}_{\text{RE},i}(t). \quad (35)$$

To make comparisons between simulations and experiments we normalize these quantities to their initial values $\mathcal{E}_{\text{RE}}(0)$ and $I_{\text{RE}}(0)$. The initial values correspond to time 1.405 ms from DIII-D discharge #164409.

The following calculations all use dynamic magnetic and electric fields unless otherwise noted, and synchrotron and bremsstrahlung radiation. We note that the role of radiation for the present study of RE dissipation by impurity injection is negligible (not shown). Table II summarizes all the simulations presented in this section, with the combination of collisional, bound electron, electric field, spatiotemporal electron and impurity density, and initial RE energy and pitch distribution models used.

A. Confinement Losses

We begin by simulating a RE beam without any collisions, which decouples the effects of deconfinement of REs due to the evolution of the experimentally-reconstructed fields from collisional effects. Fig. 8 shows such a simulation, where we indicate different initial RE beam widths in the left plot, including particles within $\psi_N < 1.0$ in dark blue, $\psi_N < 0.78$ in red, $\psi_N < 0.56$ in green, and $\psi_N < 0.34$ in light blue. This is accomplished by a single simulation with a spatially uniform RE distribution, because of the linear nature of RE orbits. The right plot in Fig. 8 shows that as the initial RE beam width gets smaller, the effect of deconfinement is delayed. Physically, the smaller radii beams will not interact with the inner wall until later times, but then will

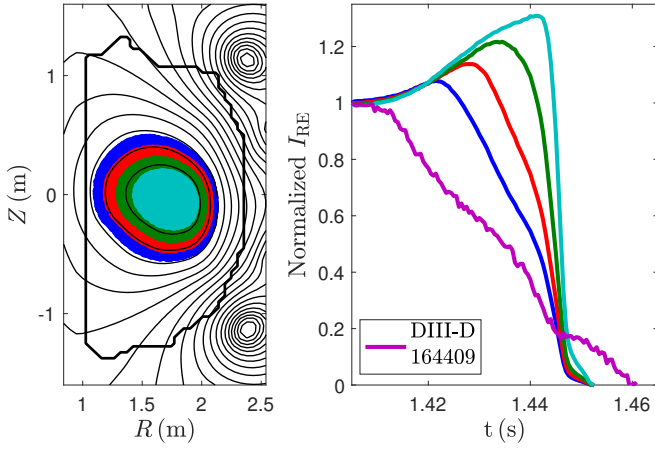


FIG. 8. Subsets of REs, delineated by initial value of poloidal flux function consistent with the left figure, to study the effect of different beam widths, made possible by the linear nature of individual RE orbits. Calculation performed consistent with Case 1 model.

have all their particles deconfined rapidly. The most extreme case would be a pencil beam, which would not lose any particles until the beam touches the wall, and then all particles would be lost nearly instantaneously. The normalized I_{RE} for each subset of simulated REs is compared to the experimental current from DIII-D discharge #164409, indicated by the violet trace.

The increase in normalized RE current is an interesting result. As the magnetic configuration evolves, the magnetic axis advects toward the HFS, decreasing the major radial location of REs summed in Eq. (35). Also noted in Ref. [40]. This makes intuitive sense, as all REs are approximately traveling at c in the toroidal direction, starting at a pitch of $\eta = 10^\circ$ with a small spread in pitch angle due to spatial orbit effects [13]. Without collisions, this speed remains the same, and as the RE beam advects toward the HFS, where the toroidal orbit length decreases linearly with R , the toroidal transit distance, and therefore time, becomes less, yielding more I_{RE} . There will also be an additional effect due to pitch angle “pinching” due to the toroidal electric field, but we find that this is a small effect compared to the major radial location (not shown).

At the time after all REs are either deconfined or thermalized in this and each of the following simulations, DIII-D discharge #164409 shows current remaining, approximately 46 kA, for an additional 10 ms. With the present modeling capabilities of KORC, we are unable to study this discrepancy directly, and will address it in future work. However, possible reasons for the remaining current include a possible lack of magnetic reconstruction fidelity, secondary REs generated by large-angle collisions during this time period of larger induced toroidal electric field, or evolution of the companion plasma. First, from the poloidal flux contours in the final plot of Fig. 2 for $t = 1.445$ s, there is an open magnetic configuration, consistent with the loss of nearly all REs at this time, except for those trapped on the low field side. It is possible that JFIT, which is only constrained to external mag-

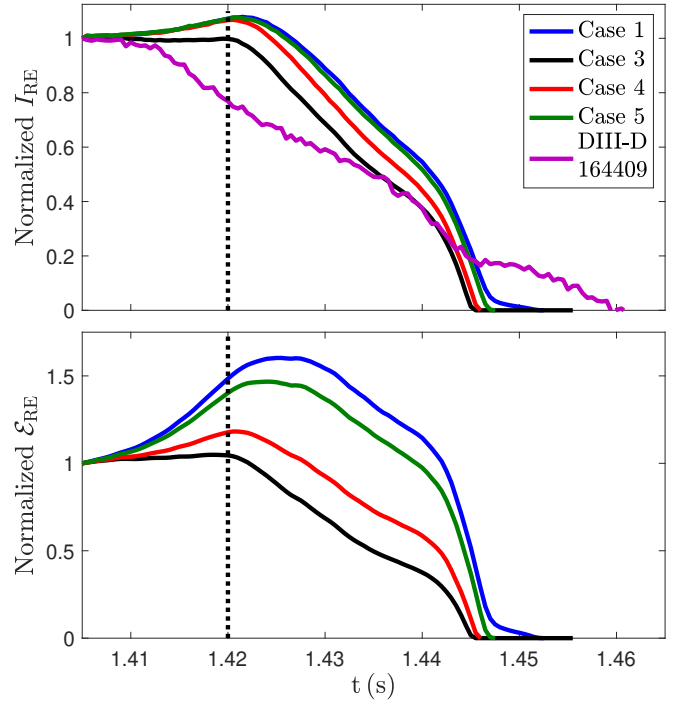


FIG. 9. Comparison of evolution of normalized RE beam current (top plot) and RE beam energy (bottom plot) for different bound electron models indicated in Table II with DIII-D discharge #164409 indicated by the violet trace. The vertical, dashed, black line indicated the approximate time that deconfinement begins to play a role, as estimated from Fig. 12.

netic diagnostics, could be incorrectly reconstructing the internal magnetic configuration, and a closed flux region could be remaining. Second, if our modeling contained a secondary RE source, these added REs would have a high probability to be generated in the trapped region, and subsequently confined. Third, from Fig. 4 there is still a significant line integrated electron density being observed on the V1 chord in the open flux region, indicating that plasma is not being rapidly deconfined as one may expect. For a crude estimate, the companion plasma could be carrying approximately 4.2 kA to 43 kA of Ohmic current, for a range of electron temperature of 1.5 eV to 8 eV, possibly making a significant contribution to the observed current. Additional study is required to better understand this final time interval of the RE dissipation.

B. Bound electron modeling

As a next step we include Coulomb collisions, and investigate the effect of different models of bound electron physics developed in Secs. IIC2 and IIC3. Figure 9 shows the dependence of the normalized RE current (top plot) and energy (bottom plot) evolution on the bound electron model. The blue trace corresponds Case 1 shown as the dark blue trace in Fig. 8, the black trace uses Case 3 with the Bound-e model from Eqs. 20a-20c, the red trace uses Case 4 with the Extra-e model from

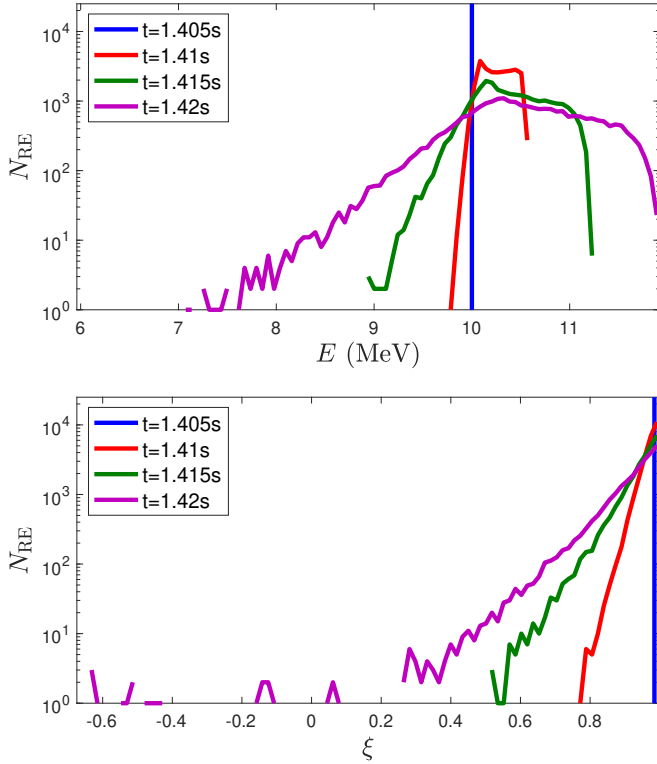


FIG. 10. Evolution of the RE ensemble energy (top plot) and cosine of the pitch angle (bottom plot) for the simulation in Fig. 9 using the Case 3 model. Traces show the distributions every 5 ms until confinement begins to degrade as estimated from Fig. 12.

Eqs. 23a-23c, the green trace uses the Case 5 with the No-Bound electron model from Eqs. 11a-11c, and the violet trace is the current from DIII-D discharge #164409. The vertical, dashed, black line indicated the approximate time that deconfinement begins to play a role, as estimated from Fig. 12. Progressing from no collisions to the No-Bound, Extra-e, and lastly Bound-e collision models, the KORC simulated normalized RE current more closely aligns with the experimental current. We note that while RE current evolution measurements are routine in tokamak experiments, evolution of the RE energy is not presently available in all discharges. Recent results in Ref. [59] show the evolution of the energy distribution, as observed using the Gamma Ray Imager [60, 61]. However, these measurements presently require a low level of HXR bremsstrahlung flux, and are not available in discharges with a high level of high-Z impurities. Future work comparing KORC simulations with discharges from this scenario would make for a good validation study.

While nearly all the KORC simulations have their normalized RE current evolve qualitatively similarly, there is great disparity in how the normalized RE energy evolves in each case. Each model has the energy increasing until after confinement is lost, with the main difference being the rate at which energy increases due to acceleration by the toroidal electric field in each case. The collisional slowing down is nonexistent in the no collisions simulation and is so weak in the No Bound model, that both cases still have energy increasing after loss of con-

finement. For these parameters, it is striking how the No-Bound electron model is barely different from no collision case, pointing to the conclusion that the inclusion of a bound electron model is essential for recovering accurate simulation results. The simulation incorporating the Bound-e model is the only one to have any current dissipate before loss of confinement, albeit at the small amount of $> 1\%$, and the least energy increase of 4.5% . The simulation using the Extra-e model yields similar results to that using the Bound-e model, but due to greatly increased pitch angle scattering, by a factor of 7.15 at 10 MeV, and marginally increased collisional friction, by a factor of 1.33 at 10 MeV, in Bound-e model, as seen in Fig. 5.

To better understand the RE ensemble averaged energy and current, it is instructive to directly view the evolution of the energy and pitch angle distributions. Figure 10 shows the evolution of the energy (top plot) and cosine of the pitch angle (bottom plot) for the simulation using the Bound-e model. Before REs begin to be deconfined, it is clear that the average energy is increasing, while ξ is decreasing, or rather η is increasing. We view ξ as compared to η , because ξ is a direct input into the calculation of the current consistent with Eq. (35). We posit that the energy is increasing due to REs being accelerated by the induced toroidal electric field more than decelerated by collisional slowing down. Comparing the approximate time rate of change of the momentum due to the induced toroidal field $dp/dt = -eE_\phi\xi$ and collisional slowing down for the initial RE energy and pitch, the electric force is initially equal to the collisional slowing down and increases as a larger toroidal electric field is induced. Conversely, we hypothesize that the pitch angle is increasing due to collisional pitch angle scattering with the Bound-e model greater than the pinching effect due to the induced toroidal electric field. Comparing the time rate of change of the cosine of the pitch angle due to the induced toroidal field $d\xi/dt = -eE_\phi(1 - \xi^2)/p$ and collisional pitch angle scattering for the initial RE energy and pitch, the collisional pitch angle scattering is approximately 10^2 larger than the electric force pinching effect.

C. Parametric Modeling

Now that we have discussed the effects of deconfinement and bound electron models, we turn our attention to the parameterization of the initial RE distribution and spatiotemporal electron and partially-ionized impurity profile. Figure 11 shows the dependence of the normalized RE current (top plot) and energy evolution (bottom plot) on the initial RE distribution and spatiotemporal density profile. The dark blue trace is Case 1 without collisions shown as the dark blue trace in Fig. 8; the dotted, dark blue trace is Case 2 without collisions or the dynamic toroidal electric field; the black trace is the canonical Case 3 using the Bound-e model shown in Fig. 9; the red trace is Case 6 that uses the initial RE energy and pitch distribution from Ref. [57]; the green trace is Case 7 using the narrow and dense spatiotemporal density pro-

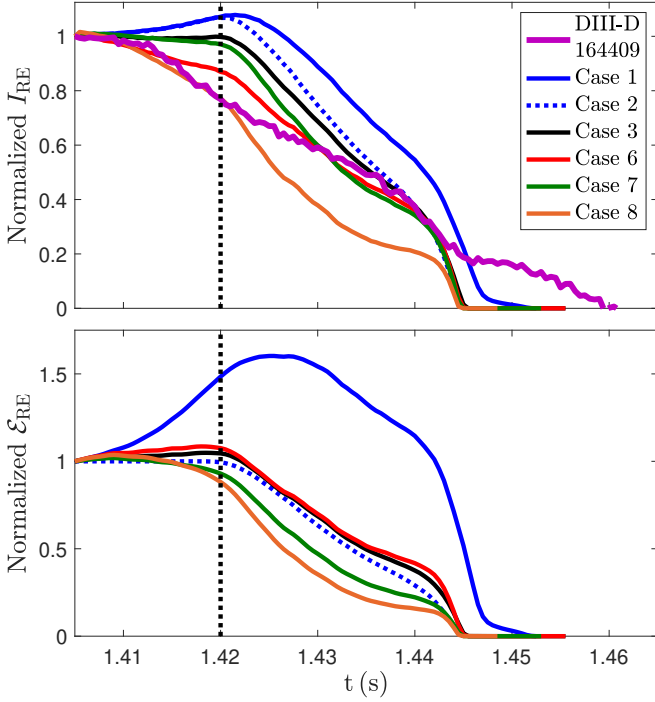


FIG. 11. Comparison of evolution of normalized RE beam current (top plot) and RE beam energy (bottom plot) for a hierarchy of models indicated in Table II with DIII-D discharge #164409 indicated by the violet trace. The vertical, dashed, black line indicated the approximate time that deconfinement begins to play a role, as estimated from Fig. 12.

file; and the orange trace is Case 8 using both the initial RE energy and pitch distribution from Ref. [57] and the narrow and dense spatiotemporal density profile.

The collisionless simulation without the induced toroidal electric field (Case 2) indicates that the effect of the toroidal electric field nearly balances out collisional dissipation, as it is nearly identical to the canonical case. This reinforces our estimation of the comparison of the two forces from the end of Sec. IV B.

It can be seen that varying the initial energy and pitch distribution has a significant effect on current dissipation but not energy dissipation. We postulate that this is due to lower initial mean energy, which yields a larger pitch angle scattering consistent with Eq. (8b) or (10) that varies as $1/p^2 \sim 1/E^2$.

Varying spatiotemporal density profile to use the narrow and dense profile has a marginal effect on current dissipation but significant effect on energy dissipation. We posit that this is due to the collisional force being approximately twice as large as the toroidal electric force for the initial conditions for the more dense spatiotemporal density profile, whereas it was approximately equal for the more diffuse spatiotemporal density profile. By itself, varying the spatiotemporal density profile decreases the normalized energy before deconfinement, but only by 7%.

When the effects of the different initial energy and pitch distribution and denser spatiotemporal density are combined, both the current and energy are dissipated to a higher degree than with either of the effects sepa-

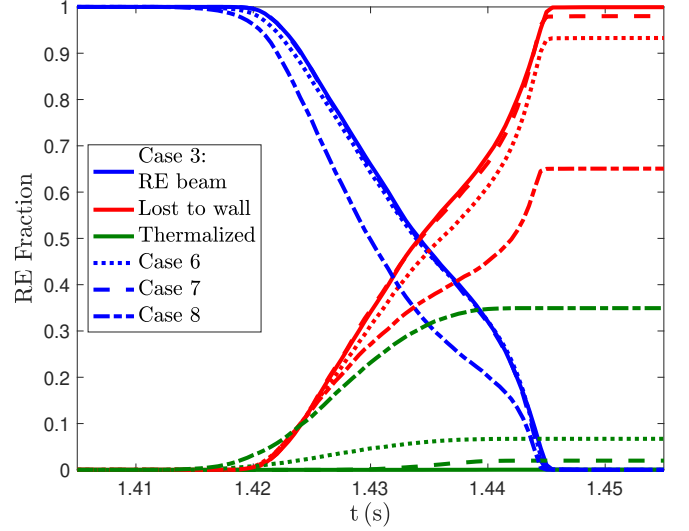


FIG. 12. Comparison of the time evolution of the number of confined REs (blue traces), deconfined REs (red traces), and collisionally dissipated REs (green traces), where the compared simulations use models given in Table II.

rately. This can be viewed as the best case scenario from the modeling of RE mitigation via Ne MGI in DIII-D discharge #164409. There is, however, a shortfall in the simulated current after confinement degrades for the case with combined effects. We hypothesize that this shortfall would be augmented by the evolution of the companion plasma or secondary REs generated by large-angle collisions during this time period of larger induced toroidal electric field. As was the case in Sec. IV A, we will discuss this further in Sec. V.

We can also view the evolution of particles in the RE beam, deconfined particles impacting the wall, and thermalized particles whose momentum fall below $p < m_e c$. Figure 12 shows the evolution of particles in the RE beam (blue traces), deconfined particles (red traces), and thermalized particles (green traces) for simulations presented in Fig. 11, where the canonical simulation is indicated with solid traces, the simulation with initial RE energy and pitch distribution from Ref. [57] indicated by the dotted traces, the simulation with the more dense spatiotemporal density profile indicated by the dashed traces, and the simulation combining both effects by the dash-dotted traces.

The previous results are borne out clearly in Fig. 12, namely that the majority of REs across all simulations are lost to the wall, rather than thermalized. The canonical simulation (Case 3) is the most dire situation with $> 0.1\%$ thermalized, the dense ST simulation has 2% thermalized, the simulation with initial RE energy and pitch distribution from Ref. [57] has 7% thermalized, and the simulation with combined effects is again the best case scenario with 35% thermalized. The simulations using initial RE energy distribution from Ref. [57] have lower average initial distribution energy, where the collisional slowing down is more effective.

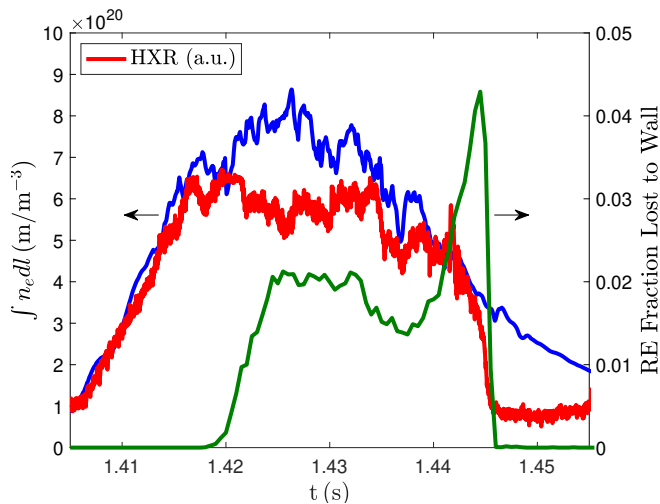


FIG. 13. Comparison between the V1 interferometer diagnostic (blue trace) and HXR signal (red trace) for DIII-D discharge #164409 with the RE fraction lost to the wall for the canonical KORC calculation (solid green trace).

D. Additional Experimental Connections

In Fig. 1d, the HXR emission is observed to increase rapidly upon the injection of Ne gas into the post-disruption RE beam. The HXR signal (red trace) has been reproduced in Fig. 13, and plotted with the line integrated electron density from vertical chord V1 (blue trace) and the simulated RE fraction lost to the wall for the canonical KORC calculation (green trace). The HXR detector observes radiation emitted by REs when striking first wall or bulk ions and neutrals in plasma, thus both sources require REs for any signal. The initial rise in HXR correlates directly with the interferometer signal. There is also good agreement between the HXR signal the deconfinement of simulated REs. The final spike in RE fraction lost to the wall is not seen in the HXR signal. This indicates that future analysis is required to determine the proportionality constants to the total HXR signal coming from RE interaction with companion plasma and with wall separately. Lastly, because the HXR signal does not fully drop to the offset value, it indicates that there are additional REs remaining after KORC simulations expect all REs to be deconfined. This is further evidence that large-angle collisions are generating additional REs when the induced toroidal electric field is large near the end of the RE beam deconfinement, and will be discussed more in Sec. V.

Because KORC evolves the momentum and location of all simulated particles, it is possible to calculate the power flux to the wall when REs are deconfined. As there are of the order 10^{16} REs in a standard RE beam for DIII-D parameters, and only 2.5×10^4 REs simulated with KORC, it is necessary to calculate a scaling factor to calculate an experimental relevant power flux. We scale the initial current from DIII-D discharge #164409 $I_0 = 2.813 \times 10^5$ A, by that calculated using Eq. (35) $I_{RE}(0) = 1.15 \times 10^{-7}$ to get a ratio of 2.45×10^{12} . In our calculations of the power flux, we assume every particle

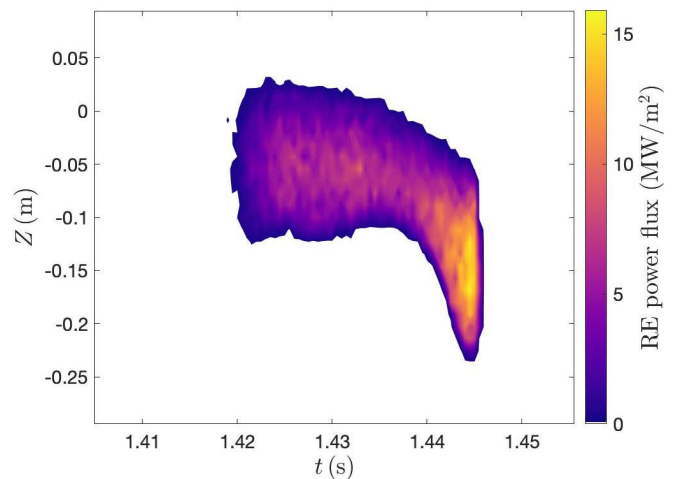


FIG. 14. Power flux on the inner wall calculated for the canonical KORC calculation. The total number of experimental REs was estimated and used to scale up the KORC calculated REs to arrive at a physically significant value. The axisymmetric magnetic field configuration leads to REs impacting the inner wall uniformly in the toroidal direction.

represents a physical number of particles equal to the calculated ratio. As the magnetic configuration is axisymmetric, so is the RE deposition on the inner wall (not shown). The power flux is calculated by binning in the Z direction in $[-0.3, 0.1]$ m, and summing up the particle energy deposited in a given bin per 0.5 ms. The calculation of the power flux varies as the spatial bin width is varied (not shown); the results presented in Fig. 14 are for 35 bins of width 1.1 cm. We note that the deposited power flux is located below the vertical midplane due to the helicity of the magnetic field in the present configuration. Future work will include comparing these deposition power fluxes to infrared camera images.

V. CONCLUSIONS AND DISCUSSION

Simulations performed with the kinetic RE code KORC incorporate experimentally-reconstructed, time-dependent magnetic and electric fields, and line integrated electron density data to construct spatiotemporal models of electron and partially-ionized impurity transport in the companion plasma. We use KORC to model DIII-D experiment #164409 that injects Ne MGI in order to mitigate a post-disruption, vertically-controlled, RE beam. Comparison of KORC results and experimental current evolution are performed including Coulomb collisions with different models of partially-ionized impurity physics, and it is found that the model presented in Ref. [7] most closely reproduce the experimental current evolution. Comparison of KORC results and experimental current evolution are performed for different models of initial RE energy and pitch angle distributions and different spatiotemporal electron and partially-ionized impurity transport. The majority of KORC calculations indicate that while the RE beam current is decreasing, the RE beam energy increases until confinement degrades.

We posit that collisional pitch angle scattering is primarily responsible for decreasing the current, while the electric field accelerates REs more than collisional friction slows them down. As current dissipates, the plasma advects toward the inner wall limiter and results in rapid deconfinement of REs, which we find is the primary dissipation mechanism, rather than collisions. Using KORC results on the RE energy when striking the first wall, we make predictions of the power flux on the inner wall during RE deconfinement.

The results presented have immediate relevance to ITER and future reactor level tokamaks. This work quantifies the efficacy of RE mitigation via injected impurities, and yields a relative importance of effects. The zeroth order effect is the dynamic magnetic field configuration that determines confinement of REs as summarized by Fig. 8 in Sec. IV A. First order effects are the inductive toroidal electric field as viewed in Fig. 11 of Sec. IV C, the partially-ionized impurity model as viewed in Fig. 9 of Sec. IV B, spatiotemporal density and partially-ionized impurity transport as viewed in Fig. 11 of Sec. IV C, and initial RE energy and pitch distribution as viewed in Fig. 11 of Sec. IV C. Synchrotron and bremsstrahlung radiation are much smaller effects for the dissipation process in DIII-D discharge #164409 and are not shown. A major contribution of the present study is the identification of the critical role played by loss of confinement in comparison with the relatively slow collisional damping.

This work is just the beginning of the necessary KORC modeling efforts toward understanding important RE spatial effects. Additional preliminary studies are underway of the spatiotemporal transport of injected impurities, separately looking at Ar injection, varying the amount of injected impurities, SPI injection technology, and injection into different tokamaks, such as JET and KSTAR. We note that the results presented here are generally in line with recent experiments at JET exploring high-Z impurity injection for RE mitigation [62, 63]. An important next development for KORC is the implementation of a large-angle collision operator. The magnetic to kinetic energy conversion by large-angle collisions upon the termination of the RE beam is an ongoing topic of research [11, 16, 64–66]. The injection of impurities provides additional electrons to knock-on [67], and the induced toroidal electric field is greatest when magnetic configuration is rapidly deconfining. The large RE losses can induce a large toroidal electric field that may increase the Ohmic current, possibly explaining the results in Secs. IV A, IV C, and IV D. Because large-angle collisions produces REs at large pitch angles [68], these REs could potentially add a significant amount of energy to the RE beam without an associated increase in current. Lastly, tight coupling with an MHD code having impurity and ablation models is ultimately necessary for robust, predictive modeling of RE evolution. Such simulations will require calculation of the self-consistent, induced electric field as the RE ensemble evolves, and the

resulting evolution of the magnetic configuration evolving with RE current and companion plasma.

ACKNOWLEDGMENTS

The authors would like to thank J. Herfindal, E. Hollmann, M. Lehnert, A. Lvovskiy, E. Nardon, C. Paz-Soldan, and R. Sweeney for their insight into post-disruption, RE experiments, L. Carbajal, M. Cianciosa, D. Green, J. Lore, H. Lu, and S. Seal for their help with the development of KORC, and J. Lore and the anonymous reviewers for their valuable comments on this manuscript.

This manuscript has been authored by UT-Battelle, LLC under Contract No. DE-AC05-00OR22725 with the U.S. Department of Energy. The United States Government retains and the publisher, by accepting the article for publication, acknowledges that the United States Government retains a non-exclusive, paid-up, irrevocable, worldwide license to publish or reproduce the published form of this manuscript, or allow others to do so, for United States Government purposes. The Department of Energy will provide public access to these results of federally sponsored research in accordance with the DOE Public Access Plan (<https://www.energy.gov/downloads/doe-public-access-plan>).

This material is based upon work supported by the U.S. Department of Energy, Office of Science, Office of Fusion Energy Sciences, using the DIII-D National Fusion Facility, a DOE Office of Science user facility, under Award DE-FC02-04ER54698. This research also uses resources of the National Energy Research Scientific Computing Center (NERSC), a U.S. Department of Energy Office of Science User Facility operated under Contract No. DE-AC02-05CH11231.

Data used to generate figures can be obtained in the digital format by following the link in Ref. [69].

DISCLAIMER

This report was prepared as an account of work sponsored by an agency of the United States Government. Neither the United States Government nor any agency thereof, nor any of their employees, makes any warranty, express or implied, or assumes any legal liability or responsibility for the accuracy, completeness, or usefulness of any information, apparatus, product, or process disclosed, or represents that its use would not infringe privately owned rights. Reference herein to any specific commercial product, process, or service by trade name, trademark, manufacturer, or otherwise, does not necessarily constitute or imply its endorsement, recommendation, or favoring by the United States Government or any agency thereof. The views and opinions of authors expressed herein do not necessarily state or reflect those of the United States Government or any agency thereof.

- [2] A. H. Boozer, *Physics of Plasmas* **22**, 032504 (2015), <https://doi.org/10.1063/1.4913582>, URL <https://doi.org/10.1063/1.4913582>.
- [3] N. Commaux, L. Baylor, T. Jernigan, E. Hollmann, P. Parks, D. Humphreys, J. Wesley, and J. Yu, *Nuclear Fusion* **50**, 112001 (2010), URL <https://doi.org/10.1088/2F0029-5515/2F50/2F11/2F112001>.
- [4] M. Lehnen, K. Aleynikova, P. Aleynikov, D. Campbell, P. Drewelow, N. Eidietis, Y. Gasparyan, R. Granetz, Y. Gribov, N. Hartmann, et al., *Journal of Nuclear Materials* **463**, 39 (2015), ISSN 0022-3115, pLASMA-SURFACE INTERACTIONS 21, URL <http://www.sciencedirect.com/science/article/pii/S0022311514007594>.
- [5] E. M. Hollmann, P. B. Aleynikov, T. Fülöp, D. A. Humphreys, V. A. Izzo, M. Lehnen, V. E. Lukash, G. Papp, G. Pautasso, F. Saint-Laurent, et al., *Physics of Plasmas* **22**, 021802 (2015), <https://doi.org/10.1063/1.4901251>, URL <https://doi.org/10.1063/1.4901251>.
- [6] L. Baylor, S. Meitner, T. Gebhart, J. Caughman, J. Herfindal, D. Shiraki, and D. Youchison, *Nuclear Fusion* **59**, 066008 (2019), URL <https://doi.org/10.1088/2F1741-4326/2Fab136c>.
- [7] L. Hesslow, O. Embréus, A. Stahl, T. C. DuBois, G. Papp, S. L. Newton, and T. Fülöp, *Phys. Rev. Lett.* **118**, 255001 (2017), URL <https://link.aps.org/doi/10.1103/PhysRevLett.118.255001>.
- [8] L. Hesslow, O. Embréus, M. Hoppe, T. C. DuBois, G. Papp, M. Rahm, and T. Fülöp, *J. Plasma Phys.* **84**, 905840605 (2018).
- [9] D. Shiraki, N. Commaux, L. Baylor, C. Cooper, N. Eidietis, E. Hollmann, C. Paz-Soldan, S. Combs, and S. Meitner, *Nuclear Fusion* **58**, 056006 (2018), URL <https://doi.org/10.1088/2F1741-4326/2Faab0d6>.
- [10] A. N. James, E. M. Hollmann, and G. R. Tynan, *Review of Scientific Instruments* **81**, 10E306 (2010), <https://doi.org/10.1063/1.3475710>, URL <https://doi.org/10.1063/1.3475710>.
- [11] E. Hollmann, M. Austin, J. Boedo, N. Brooks, N. Commaux, N. Eidietis, D. Humphreys, V. Izzo, A. James, T. Jernigan, et al., *Nuclear Fusion* **53**, 083004 (2013), URL <https://doi.org/10.1088/2F0029-5515/2F53/2F8/2F083004>.
- [12] E. Hollmann, P. Parks, D. Humphreys, N. Brooks, N. Commaux, N. Eidietis, T. Evans, R. Isler, A. James, T. Jernigan, et al., *Nuclear Fusion* **51**, 103026 (2011), URL <https://doi.org/10.1088/2F0029-5515/2F51/2F10/2F103026>.
- [13] L. Carbajal, D. del Castillo-Negrete, D. Spong, S. Seal, and L. Baylor, *Physics of Plasmas* **24**, 042512 (2017), <https://doi.org/10.1063/1.4981209>, URL <https://doi.org/10.1063/1.4981209>.
- [14] P. Aleynikov, K. Aleynikova, B. Breizman, G. Huijsmans, S. Kononov, S. Putvinski, and V. Zhogolev, in *Proc. of the 25th IAEA Fusion Energy Conference* (IAEA, Vienna, 2014), St. Petersburg, Russia, tH/P3-38.
- [15] S. Kononov, P. Aleynikov, K. Aleynikova, Y. Gribov, R. Ismailov, A. Ivanov, R. Khayrutdinov, D. Kiramov, M. Lehnen, V. Leonov, et al., in *Proc. of the 26th IAEA Fusion Energy Conference* (IAEA, Vienna, 2016), Kyoto, Japan, tH/7-1.
- [16] J. Martín-Solís, A. Loarte, and M. Lehnen, *Nuclear Fusion* **57**, 066025 (2017), URL <https://doi.org/10.1088/2F1741-4326/2Faa6939>.
- [17] C. Reux, V. Plyusnin, B. Alper, D. Alves, B. Bazylev, E. Belonohy, A. Boboc, S. Brezinsek, I. Coffey, J. Decker, et al., *Nuclear Fusion* **55**, 093013 (2015), URL <https://doi.org/10.1088/2F0029-5515/2F55/2F9/2F093013>.
- [18] D. A. Spong, D. del Castillo-Negrete, L. C. Gomez, C. Lau, D. P. Brennan, C. Liu, C. Collins, C. Paz-Soldan, M. A. V. Zeeland, K. E. Thome, et al., in *Proc. of the 27th IAEA Fusion Energy Conference* (IAEA, Vienna, 2018), Ahmedabad, India, tH/P8-17.
- [19] D. del Castillo-Negrete, L. Carbajal, D. Spong, and V. Izzo, *Physics of Plasmas* **25**, 056104 (2018), <https://doi.org/10.1063/1.5018747>, URL <https://doi.org/10.1063/1.5018747>.
- [20] G. Papp, M. Drevlak, T. Fülöp, and P. Helander, *Nuclear Fusion* **51**, 043004 (2011), URL <https://doi.org/10.1088/2F0029-5515/2F51/2F4/2F043004>.
- [21] G. Papp, M. Drevlak, T. Fülöp, P. Helander, and G. I. Pokol, *Plasma Physics and Controlled Fusion* **53**, 095004 (2011), URL <https://doi.org/10.1088/2F0741-3335/2F53/2F9/2F095004>.
- [22] C. Sommariva, E. Nardon, P. Beyer, M. Hoelzl, G. Huijsmans, D. van Vugt, and JET Contributors, *Nuclear Fusion* **58**, 016043 (2017), URL <https://doi.org/10.1088/2F1741-4326/2Faa95cd>.
- [23] C. Sommariva, E. Nardon, P. Beyer, M. Hoelzl, G. Huijsmans, and JET Contributors, *Nuclear Fusion* **58**, 106022 (2018), URL <https://doi.org/10.1088/2F1741-4326/2Faad47d>.
- [24] V. Izzo, E. Hollmann, A. James, J. Yu, D. Humphreys, L. Lao, P. Parks, P. Sieck, J. Wesley, R. Granetz, et al., *Nuclear Fusion* **51**, 063032 (2011), URL <https://doi.org/10.1088/2F0029-5515/2F51/2F6/2F063032>.
- [25] Z. H. Jiang, J. Huang, R. H. Tong, T. T. Yang, Z. F. Lin, V. Izzo, C. H. Li, Y. F. Liang, X. Ye, Y. H. Ding, et al., *Physics of Plasmas* **26**, 062508 (2019), <https://doi.org/10.1063/1.5100093>, URL <https://doi.org/10.1063/1.5100093>.
- [26] C. J. McDevitt, Z. Guo, and X.-Z. Tang, *Plasma Physics and Controlled Fusion* **61**, 024004 (2019), URL <https://doi.org/10.1088/2F1361-6587/2Faaf4d1>.
- [27] Y. Liu, P. Parks, C. Paz-Soldan, C. Kim, and L. Lao, *Nuclear Fusion* **59**, 126021 (2019), URL <https://doi.org/10.1088/2F1741-4326/2Fab3f87>.
- [28] L. Carbajal, D. del Castillo-Negrete, and J. J. Martinell, *Physics of Plasmas* **27**, 032502 (2020), <https://doi.org/10.1063/1.5135588>, URL <https://doi.org/10.1063/1.5135588>.
- [29] D. Whyte, T. Jernigan, D. Humphreys, A. Hyatt, C. Lasnier, P. Parks, T. Evans, P. Taylor, A. Kellman, D. Gray, et al., *Journal of Nuclear Materials* **313-316**, 1239 (2003), ISSN 0022-3115, plasma-Surface Interactions in Controlled Fusion Devices 15, URL <http://www.sciencedirect.com/science/article/pii/S0022311502015258>.
- [30] E. Nardon, A. Fil, P. Chauveau, P. Tamain, R. Guirlet, H. Koslowski, M. Lehnen, C. Reux, F. Saint-Laurent, and JET Contributors, *Nuclear Fusion* **57**, 016027 (2016), URL <https://doi.org/10.1088/2F0029-5515/2F57/2F1/2F016027>.
- [31] E. Hollmann, N. Eidietis, J. Herfindal, P. Parks, A. Pigarov, D. Shiraki, M. Austin, L. Bardoczi, L. Baylor, I. Bykov, et al., *Nuclear Fusion* **59**, 106014 (2019), URL <https://doi.org/10.1088/2F1741-4326/2Fab32b2>.
- [32] L. Carbajal and D. del Castillo-Negrete, *Plasma Physics and Controlled Fusion* **59**, 124001 (2017), URL <https://doi.org/10.1088/2F1361-6587/2Faa883e>.
- [33] X. Tao, A. A. Chan, and A. J. Brizard, *Phys. Plasmas* **14**, 092107 (2007), <https://doi.org/10.1063/1.2773702>, URL <https://doi.org/10.1063/1.2773702>.

- [34] J. R. Cary and A. J. Brizard, *Rev. Mod. Phys.* **81**, 693 (2009), URL <https://link.aps.org/doi/10.1103/RevModPhys.81.693>.
- [35] J. R. Cash and A. H. Karp, *ACM Trans. Math. Softw.* **16**, 201 (1990), ISSN 0098-3500, URL <http://doi.acm.org/10.1145/79505.79507>.
- [36] D. A. Humphreys and A. G. Kellman, *Physics of Plasmas* **6**, 2742 (1999), <https://doi.org/10.1063/1.873231>, URL <https://doi.org/10.1063/1.873231>.
- [37] L. L. Lao, J. R. Ferron, R. J. Groebner, W. Howl, H. S. John, E. J. Strait, and T. S. Taylor, *Nucl. Fusion* **30**, 1035 (1990).
- [38] F. M. Levinton, R. J. Fonck, G. M. Gammel, R. Kaita, H. W. Kugel, E. T. Powell, and D. W. Roberts, *Phys. Rev. Lett.* **63**, 2060 (1989).
- [39] A. Pletzer and D. McCune, *Ntcc pspline module* (2010), URL <https://w3.pppl.gov/ntcc/PSPLINE/>.
- [40] N. W. Eidietis, N. Commaux, E. M. Hollmann, D. A. Humphreys, T. C. Jernigan, R. A. Moyer, E. J. Strait, M. A. VanZeeland, J. C. Wesley, and J. H. Yu, *Physics of Plasmas* **19**, 056109 (2012), <https://doi.org/10.1063/1.3695000>, URL <https://doi.org/10.1063/1.3695000>.
- [41] D. Hu and H. Qin, *Physics of Plasmas* **23**, 032510 (2016), <https://doi.org/10.1063/1.4944934>, URL <https://doi.org/10.1063/1.4944934>.
- [42] A. Trubnikov, in *Reviews of Plasma Physics*, edited by M. A. Leontovich (Consultants Bureau, New York, 1965), vol. 1, p. 105.
- [43] C. W. Gardiner, *Stochastic Methods* (Springer-Verlag, Berlin, Heidelberg, 2004).
- [44] C. F. F. Karney and N. J. Fisch, *The Physics of Fluids* **28**, 116 (1985), <https://aip.scitation.org/doi/pdf/10.1063/1.865191>, URL <https://aip.scitation.org/doi/abs/10.1063/1.865191>.
- [45] H. Bethe, *Annalen der Physik* **397**, 325 (1930), (in German), <https://onlinelibrary.wiley.com/doi/pdf/10.1002/andp.19303970303>, URL <https://onlinelibrary.wiley.com/doi/abs/10.1002/andp.19303970303>.
- [46] S. P. A. Sauer, J. Oddershede, and J. R. Sabin, in *Concepts of Mathematical Physics in Chemistry: A Tribute to Frank E. Harris - Part A*, edited by J. R. Sabin and R. Cabrera-Trujillo (Academic Press, 2015), vol. 71 of *Advances in Quantum Chemistry*, pp. 29 – 40, URL <http://www.sciencedirect.com/science/article/pii/S0065327615000027>.
- [47] V. D. Kirillov, B. A. Trubnikov, and S. A. Trushin, *Fiz. Plazmy* **1**, 218 (1975).
- [48] V. Zhogolev and S. Konovalov, *VANT or Problems of Atomic Sci. and Tech. series Thermonuclear Fusion* **37**, 71 (2014), (in Russian).
- [49] M. Rosenbluth and S. Putvinski, *Nucl. Fusion* **37**, 1355 (1997), URL <http://stacks.iop.org/0029-5515/37/i=10/a=I03>.
- [50] L. D. Landau and E. M. Lifshitz, *The Classical Theory of Fields* (Pergamon Press, 1971), 3rd ed.
- [51] J. D. Jackson, *Classical Electrodynamics* (Wiley, 1962).
- [52] E. Hirvijoki, J. Decker, A. J. Brizard, and O. Embréus, *J. Plasma Phys.* **81**, 475810504 (2015).
- [53] M. Bakhtiari, G. J. Kramer, M. Takechi, H. Tamai, Y. Miura, Y. Kusama, and Y. Kamada, *Phys. Rev. Lett.* **94**, 215003 (2005), URL <https://link.aps.org/doi/10.1103/PhysRevLett.94.215003>.
- [54] O. Embréus, A. Stahl, and T. Fülöp, *New Journal of Physics* **18**, 093023 (2016), URL <https://doi.org/10.1088%2F1367-2630%2F18%2F9%2F093023>.
- [55] N. Metropolis, A. W. Rosenbluth, M. N. Rosenbluth, A. H. Teller, and E. Teller, *The Journal of Chemical Physics* **21**, 1087 (1953), <https://doi.org/10.1063/1.1699114>, URL <https://doi.org/10.1063/1.1699114>.
- [56] W. K. Hastings, *Biometrika* **57**, 97 (1970), ISSN 00063444, URL <http://www.jstor.org/stable/2334940>.
- [57] E. M. Hollmann, P. B. Parks, N. Commaux, N. W. Eidietis, R. A. Moyer, D. Shiraki, M. E. Austin, C. J. Lasnier, C. Paz-Soldan, and D. L. Rudakov, *Physics of Plasmas* **22**, 056108 (2015), <https://aip.scitation.org/doi/pdf/10.1063/1.4921149>, URL <https://aip.scitation.org/doi/abs/10.1063/1.4921149>.
- [58] J. Connor and R. Hastie, *Nuclear Fusion* **15**, 415 (1975), URL <https://doi.org/10.1088%2F0029-5515%2F15%2F3%2F007>.
- [59] A. Lvovskiy, C. Paz-Soldan, N. W. Eidietis, P. Aleynikov, M. E. Austin, A. D. Molin, Y. Q. L. abd R. A. Moyer, M. Nocente, D. Shiraki, L. Giacomelli, et al., *Nuclear Fusion* **60**, 056008 (2020), URL <https://doi.org/10.1088%2F1741-4326%2Fab78c7>.
- [60] C. M. Cooper, D. C. Pace, C. Paz-Soldan, N. Commaux, N. W. Eidietis, E. M. Hollmann, and D. Shiraki, *Review of Scientific Instruments* **87**, 11E602 (2016), <https://aip.scitation.org/doi/pdf/10.1063/1.4961288>, URL <https://aip.scitation.org/doi/abs/10.1063/1.4961288>.
- [61] D. C. Pace, C. M. Cooper, D. Taussig, N. W. Eidietis, E. M. Hollmann, V. Riso, M. A. Van Zeeland, and M. Watkins, *Review of Scientific Instruments* **87**, 043507 (2016), <https://doi.org/10.1063/1.4945566>, URL <https://doi.org/10.1063/1.4945566>.
- [62] C. Reux, Private Communication.
- [63] M. Lehnén, Private Communication.
- [64] S. Putvinski, P. Barabaschi, N. Fujisawa, N. Putvinskaya, M. N. Rosenbluth, and J. Wesley, *Plasma Physics and Controlled Fusion* **39**, B157 (1997), URL <https://doi.org/10.1088%2F0741-3335%2F39%2F12b%2F013>.
- [65] A. Loarte, V. Riccardo, J. Martín-Solís, J. Paley, A. Huber, M. Lehnén, and JET-EFDA Contributors, *Nuclear Fusion* **51**, 073004 (2011), URL <https://doi.org/10.1088%2F0029-5515%2F51%2F7%2F073004>.
- [66] J. Martín-Solís, A. Loarte, E. Hollmann, B. Esposito, V. Riccardo, FTU, DIII-D Team, and JET-EFDA Contributors, *Nuclear Fusion* **54**, 083027 (2014), URL <https://doi.org/10.1088%2F0029-5515%2F54%2F8%2F083027>.
- [67] L. Hesslow, O. Embréus, O. Vallhagen, and T. Fülöp, *Nuclear Fusion* **59**, 084004 (2019), URL <https://doi.org/10.1088%2F1741-4326%2Fab26c2>.
- [68] O. Embréus, A. Stahl, and T. Fülöp, *J. Plasma Phys.* **84**, 905840102 (2018).
- [69] URL https://github.com/ORNL-Fusion/KORC/tree/master/Publication_Data/Beidler_POP_2020.